

Pitch Angle Distribution of MeV Electrons in the Magnetosphere of Jupiter

Q. Nénon¹, L. P. Miller² , P. Kollmann³ , L. Liuzzo⁴ , M. Pinto⁵ , and O. Witasse⁵

¹Institut de Recherche en Astronomie et Planétologie, CNRS-UPS-CNES, Toulouse, France, ²Fundamental Technologies LLC, Lawrence, KS, USA, ³John Hopkins University – The Applied Physics Laboratory, Laurel, MD, USA, ⁴University of California Berkeley – Space Sciences Laboratory, Berkeley, CA, USA, ⁵European Space Agency, European Space Research and Technology Centre, Noordwijk, The Netherlands

Key Points:

- The Pitch Angle Distribution of MeV electron fluxes, as observed by the Galileo instrumentation, is isotropic within a factor of 3
- MeV electrons have persistent pancake shapes at $L \sim 9$, and pancake, isotropic, and scattered field-aligned distributions at $L = 15$ –60
- The field-aligned distributions may be generated by outward adiabatic radial transport or auroral acceleration

Supporting Information:

Supporting Information may be found in the online version of this article.

Correspondence to:

Q. Nénon,
q.nenon@gmail.com

Citation:

Nénon, Q., Miller, L. P., Kollmann, P., Liuzzo, L., Pinto, M., & Witasse, O. (2022). Pitch angle distribution of MeV electrons in the magnetosphere of Jupiter. *Journal of Geophysical Research: Space Physics*, 127, e2022JA030627. <https://doi.org/10.1029/2022JA030627>

Received 6 MAY 2022
Accepted 27 JUL 2022

The copyright line for this article was changed on 8 SEP 2022 after original online publication.

© 2022. The Authors.

This is an open access article under the terms of the [Creative Commons Attribution License](https://creativecommons.org/licenses/by/4.0/), which permits use, distribution and reproduction in any medium, provided the original work is properly cited.

Abstract The magnetosphere of Jupiter harbors the most extreme fluxes of MeV electrons in the solar system and therefore provides a testbed of choice to understand the origin, transport, acceleration, and loss of energetic electrons in planetary magnetospheres. Along this objective, the Pitch Angle Distribution (PAD) of energetic electrons may reveal signatures of the dominant physical processes. Here, we analyze for the first time the PAD of MeV electrons observed by the Galileo-Energetic Particle Detector (EPD) experiment in orbit around Jupiter from 1995 to 2003. We find that the MeV electron PADs observed by the integral channels of EPD appear relatively isotropic with a flux anisotropy lower than a factor of 3. Due to the relatively large angular apertures of the EPD telescopes, the actual anisotropy may be larger than the observed one. The fine anisotropy observed by Galileo-EPD reveals persistent pancake distributions at the M-shell of $M = 9$. Outward of this distance, at $M = 15$ and $M = 20$ –60, MeV electron distributions have pancake, isotropic, and scattered beam field-aligned distributions. The scattered beam distributions can either be evidence of outward adiabatic transport or may suggest that high-latitude auroral acceleration can transiently supply as much trapped MeV electrons to the middle magnetosphere as the inward adiabatic transport of electrons from an outer equatorial reservoir.

1. Introduction

In this article, the terminology “keV electrons” and “MeV electrons” designate electrons with kinetic energies greater than 1 keV and 1 MeV, respectively. A 10 MeV electron is for instance labeled as “MeV electron”. We also use the terminology “M” or “M-shell” to describe the distance of the apex of a realistic magnetic field line to the center of a planet, normalized by the planet radius. The “M-shell” naming has been introduced by the Juno mission team to highlight that the apex distance is computed by taking account a realistic magnetic field geometry rather than a dipole. In this article, realistic magnetic field lines are computed using the internal magnetic field model VIP4 (Connerney et al., 1998) combined with the current sheet model of Khurana and Schwarzl (2005).

The magnetosphere of Jupiter is the most powerful accelerator of electrons in the solar system (Mauk & Fox, 2010), with large fluxes of MeV electrons continuously present everywhere, both at low and high latitudes, from $M = 1.1$ (e.g., Nénon et al., 2018) up to $M = 100$ (e.g., Kollmann et al., 2018). Understanding how Jupiter accelerates and transports electrons in such an efficient manner despite many sink processes is important to develop a universal understanding of planetary radiation belts. Furthermore, the characterization and understanding of the Jovian energetic electrons are critical for the assessment of radiation risk for artificial satellites (e.g., Carlton et al., 2018; de Soria-Santacruz et al., 2016; Garrett & Jun 2021; Sicard-Piet et al., 2011), and for the study of moon surface weathering (Nordheim et al., 2018; Paranicas et al., 2021).

The first step toward understanding the origin and dynamics of energetic electrons at Jupiter lies in the analysis of available observations, which can either exhibit direct signatures of the physical processes at work (e.g., Kollmann et al., 2018), or can present a complex mix of different mechanism contributions, against which physics-based models can be compared (e.g., Nénon et al., 2017). At a given time and position in the magnetosphere, the energetic electron distribution can be described with the two quantities of the energy spectrum of electron fluxes and the electron Pitch Angle Distribution (PAD).

For the electron spectrum, Kollmann et al. (2018) have shown that electron acceleration due to either adiabatic radial transport or local acceleration would leave distinct signatures in the spectral parameters. Specifically, the

previous authors investigated the radial profile of certain macroscopic characteristics of the electron spectrum (the spectrum slope and cutoff energy) at $M > 20$ and revealed in this way that the acceleration of electrons is likely dominated by adiabatic radial transport in this region.

PADs can also hold clues about the physics of energetic electrons. Indeed, physical processes can have a sufficiently strong influence on an initial PAD to leave a clear signature of the mechanism at work. For instance, a pancake PAD which peaks at a pitch angle of 90° , also known as a ‘trapped distribution’, can result from the conservation of the two first adiabatic invariants during inward adiabatic radial transport and the subsequent pitch-angle dependent adiabatic acceleration. A pancake PAD may also be the manifestation of wave-particle interaction, either local acceleration of equatorial electrons (e.g., Li et al., 2016) or pitch angle scattering which can create flat-top distributions (e.g., Ma et al., 2020) that can appear as pancake if observed with a coarse angular resolution.

Field-aligned distributions, with maxima at 0° and 180° , can be divided in two categories defined by Mauk and Saur (2007) as (a) auroral beams or “true” beams which are highly collimated around the directions parallel and anti-parallel to the magnetic field and display a sharp reduction in flux when the pitch angle goes from the parallel or anti-parallel direction to 90° , and (b) field-aligned distributions or ‘scattered beams’ which exhibit a more gradual reduction of fluxes when sweeping directions from aligned to perpendicular to the magnetic field.

True field-aligned auroral beams likely show the signature of high-latitude auroral acceleration mechanisms. A scattered beam may however be the signature of one of the 4 following physical phenomena in the middle and outer magnetosphere of Jupiter:

1. A scattered beam can be a true auroral beam which has been scattered over time by an unknown process at the M-shell where the auroral beam was produced, or may have been scattered and accelerated during adiabatic inward radial transport
2. The pitch angle dependency of the loss rate associated with moon absorption can create field-aligned distributions (Long et al., 2022), as seen for energetic ions close to Jupiter (Roussos et al., 2022)
3. The loss or cooling of energetic electrons due to interaction with equatorial neutral gas or cold plasma populations may also create energetic electron field-aligned distributions (Clark et al., 2014), although physics-based modeling indicates that these processes are likely negligible for energetic electrons in the Jovian magnetosphere (Nénon et al., 2017)
4. Outward adiabatic radial transport with conservation of the two first adiabatic invariants of energetic electrons can create field-aligned distributions (e.g., Rymer et al., 2008).

In this paragraph, we explore if outward adiabatic transport is possible in the Jovian magnetosphere. Three main drivers of adiabatic radial transport have been identified at Jupiter. Firstly, injection events transport energetic electrons inward, not outward (e.g., Mauk et al., 1999). Secondly, radial diffusion may transport particles outward if the radial profile of electron phase space density (PSD) exhibits a negative slope (PSD decreasing with increasing M), for instance due to a PSD peak created by local acceleration at $M = 10$ (Woodfield et al., 2014). Garrett and Jun (2021) have shown with Galileo measurements that the long-term trend of MeV electron PSDs is a positive slope PSD radial profile, which would lead to inward radial diffusion. At lower kinetic energies, Ma et al. (2021) have shown with Juno data that electron PSD profiles are almost flat at $M > 15$, so one cannot conclude if the net effect of radial diffusion would be inward or outward transport. However, the reported long-term trends do not preclude the existence of transient negative slope PSD profiles that can lead to transient outward radial diffusion. Finally, energetic electrons can be adiabatically transported by a putative convective dawn-to-dusk electric field (Han et al., 2018). In the magnetosphere of Saturn, Hao et al. (2020) have shown that the convective electric field adiabatically transport some energetic electrons inward and others outward, depending on their energy, pitch angle, M , and local time or longitude (see their Figure 3).

In summary, far from the M-shells intercepted by the moons, a scattered field-aligned distribution may reveal either (a) the scattering of a high-latitude auroral source, (b) outward adiabatic transport due to radial diffusion associated with a negative slope in the PSD radial profile, or (c) outward adiabatic transport by a convective electric field.

Energetic electron butterfly PADs (with flux minima at 0° , 90° , and 180°) can be generated by local wave-driven acceleration (e.g., Yuan et al., 2021). A butterfly PAD can also be caused by interactions with equatorial moons, rings, neutral tori, and cold plasma disk, that is, the same process that can create field-aligned distributions.

Table 1
Galileo-EPD Electron Measurement Channels

Channel name	Energy passband (center energy)	Telescope opening angle	Number of angular sectors in real-time mode	Number of angular sectors in record mode
E0	15–29 (21) keV	15°	6	64
E1	29–42 (35) keV	15°	16	64
E2	42–55 (48) keV	15°	6	32
E3	55–93 (72) keV	15°	6	32
F0	93–188 (132) keV	15°	6	32
F1	174–304 (230) keV	15°	6	32
F2	304–527 (400) keV	15°	16	32
F3	527–884 (683) keV	15°	6	32
B1	>1 MeV ^a	15°	1	16
DC2	>1 MeV ^a	45°	1	16
DC3	>10 MeV ^a	45°	1	16

Note. Energy passbands of the E-F channels are provided by Kollmann et al. (2019).

^aThe response function of the three integral channels are given in Jun et al. (2002).

Finally, an isotropic electron distribution may reveal the dominant role of a pitch angle scattering mechanism, for instance linked to interaction with waves. Equatorial magnetic curvature scattering can also scatter electrons when the electron gyro-radius becomes comparable with the equatorial magnetic field curvature. However, this process may be inefficient in the Jovian magnetosphere for keV and MeV energetic electrons (Birmingham, 1982, 1984).

From 1995 to 2003, the Energetic Particle Detector (EPD) experiment onboard NASA's Galileo mission observed the energy spectrum and PAD of energetic electrons. This dataset remains unique and unprecedented even compared to contemporary observations by Juno, because: (a) the equatorial orbit of Galileo enabled EPD to sample most of the equatorial PAD at all times, and (b) Galileo-EPD was designed to observe energetic electrons with kinetic energies greater than 1 MeV, unlike the Juno instrumentation.

In this article, we analyze for the first time the PAD of MeV electrons (specifically >1 MeV and >10 MeV) observed by Galileo-EPD in the magnetosphere of Jupiter. The PAD of MeV electrons will be contrasted with the anisotropy of lower energy electrons (20–700 keV). Section 2 starts with a description of the Galileo-EPD design and operational modes which is necessary to introduce the state of the art of previous investigations of Galileo-EPD PADs. Section 2 also discusses electron PADs observed by other missions, including the Juno orbiter. Section 3 presents the considered dataset and the method adopted to analyze the Galileo-EPD electron PADs. Section 4 reports the PADs observed by EPD. Finally, Section 5 summarizes our findings and discusses their implications on our understanding of the physical processes

that regulate MeV electrons in the Jovian magnetosphere. Implications for spacecraft safety and moon surface weathering are also presented.

2. State of the Art of Energetic Electron PADs in the Jovian Magnetosphere

2.1. Galileo-EPD and Previous Analysis of Galileo-EPD Electron PADs

The Galileo EPD experiment is described in detail in Williams et al. (1992) and Kollmann et al. (2019). EPD comprised two subsystems, the Composition Measurement System (CMS), which was dedicated solely to ion observations, and the Low Energy Magnetospheric Measurements System (LEMMS), which was designed to observe energetic electrons and ions. LEMMS was a double-ended experiment and binned electron counts in eight differential measurement channels and three integral channels, the characteristics of which are given in Table 1. The low-energy end of LEMMS (LEMMS-LET) had a full opening angle of 15° and recorded the measurements of the eight differential channels and that of the B1 > 1 MeV integral channel. The high-energy end (LEMMS-HET) had an opening angle of 45° and observed the two integral channels DC2 (>1 MeV) and DC3 (>10 MeV).

Monte Carlo simulations of the response of the EPD measurement channels have shown that the B1 channel responds solely to >1 MeV electrons and not to protons (Jun et al., 2002). DC2 mixes particle species and can observe >1 MeV electrons and >20 MeV protons. DC3 can detect >10 MeV electrons (>11 MeV electrons according to previous work, the naming >10 MeV is used here for simplicity) and >60 MeV protons. In this article, we assume that the PADs observed by B1, DC2, and DC3 reveal the anisotropy of MeV electrons in the Jovian magnetosphere. Two caveats follow this assumption: (a) the DC2 and DC3 channels may respond to protons, and (b) the integral channels may respond to different kinetic energy ranges when sampling different pitch angles. On the second point, there is a priori no reason to expect field-aligned beams to have the same energy spectrum as equatorial electrons bouncing near the magnetic equator. The counts observed by an integral channel may therefore be dominated by electrons in the kinetic energy range [a,b] when looking at field-aligned electrons, and may respond to [c,d] electrons when looking at equatorial electrons, with a, b, c, and d possibly different. The observed anisotropy would in this case not reveal the PAD of energetic electrons but would instead show that electron distributions with different pitch angles have different spectral slopes. However, the two aforementioned

caveats are mitigated by cross comparing the PADs observed by the three integral channels. B1 will tell us if DC2 responds to electrons or protons and the detection of a PAD shape seen across the three channels would indicate that the integral channels inform on MeV electron PADs. For instance, Yuan et al. (2021) worked with integral electron channel PADs at Saturn and found butterfly distributions in all measurement channels.

EPD was installed on the spinning platform of Galileo which completed a 360° rotation about every 20 s. In order to observe the entire 4 π -steradians sky, EPD was rotated by a dedicated stepping motor with 8 discrete positions (numbered 0 to 7). Typical EPD operations kept a fixed motor position during one Galileo spin, and then changed the motor position to a nearby one for the next Galileo spin.

Galileo-EPD had two Data Acquisition Modes

1. The slow survey “real-time” mode, which accumulated electron measurements at a low cadence and in a limited number of angular sectors. The typical time resolution was of about 10–12 min Table 1 shows that real-time data for >1 MeV electrons (B1, DC2, DC3 channels) were omnidirectional and therefore do not inform on MeV electron PAD.
2. The high-cadence “record” mode, which accumulated electron fluxes in 64, 32, or 16 sectors (Table 1) with time resolutions lower than 1.4 s. Here, the number of angular sectors actually gives the number of data points collected per Galileo spin, that is, the 16-sector product gives 16 direction-resolved measurements per 20-s Galileo spin. The major drawback of the record-mode dataset is its extremely sparse coverage in time and space (see Section 3.2), due to the limited telemetry available for Galileo.

We detail hereafter previous efforts which dealt with the analysis of direction-resolved real-time and record-mode EPD electron data in order to not only introduce advances enabled by previous analysis of EPD electron PADs, but to also highlight that the B1, DC2, and DC3 >1 MeV PADs have not been analyzed to date.

2.1.1. Previous Work With Real-Time Omnidirectional Data

The 11-min averaged omnidirectional real-time product has been extensively used to develop empirical models of the Jovian radiation environment (e.g., de Soria-Santacruz et al., 2016; Sicard-Piet et al., 2011). Garrett and Jun (2021) computed the phase space density of equatorial electrons from the omnidirectional data product by assuming that electron PADs are isotropic. Kollmann et al. (2018) relied on the same isotropy assumption to study the real-time energy spectra of equatorial electrons. The isotropy assumption will be verified in this article by analyzing MeV electron PADs.

2.1.2. Previous Work With Real-Time Direction-Resolved PADs

Table 1 shows that real-time data was binned in less than 6 angular sectors for most electron channels, except for the E1 (29–42 keV) and F2 (304–527 keV) channels which accumulated real-time measurements in 16 sectors. Tomás et al. (2004) analyzed the real-time E1 and F2 data available during most of the Galileo mission. They showed that the energetic electron PADs are generally isotropic or field-aligned in the outer magnetosphere and transition to pancake distributions at a distance to the center of Jupiter varying from 10 R_j to 17 R_j (1 R_j = 71,492 km). The existence of this PAD transition has been confirmed with <1 MeV Juno measurements gathered near the magnetic equator (Ma et al., 2021). In the present study, we will investigate if this transition also exists for >1 MeV electron PADs. A similar regime transition of electron PADs was observed by Cassini at Saturn, with electron PADs mostly field-aligned or isotropic outward of $M = 11$ and pancake inward of this limit, but with butterfly distributions also present at $M \sim 8$ –11 and $M \sim 3$ (Carbary et al., 2011; Clark et al., 2014; Yuan et al., 2021). Finally, Katoh et al. (2011) conducted a survey of EPD real-time PADs observed by the E1 (29–42 keV) channel of Galileo-EPD.

2.1.3. Real-Time and Record Mode Direction-Resolved PADs

Bhattacharya et al. (2001) studied the electron PADs observed by the real-time mode and record mode of EPD for measurement channels with kinetic energies lower than ~700 keV (E and F channels). The previous authors identified when isotropic or field-aligned distributions were present and then used the observed fluxes to estimate the flux of electrons precipitating in the Jovian atmosphere in order to investigate if energetic electron precipitation could be the origin of the Jovian diffuse aurora. The direct observations of the atmospheric loss cone by Juno (Li et al., 2021) supersede these Galileo results that relied on the strong assumption that the EPD flux was representative of the downward precipitating flux.

2.1.4. Record Mode Direction-Resolved PADs

The record-mode of EPD was activated during almost all close encounters with moons. Previous work investigated the PAD of electrons close to Io (e.g., Thorne et al., 1999; Williams & Thorne, 2003), Europa (Paranicas et al., 2000), and Ganymede (e.g., Eviatar et al., 2000; Williams, 2004; Williams, Mauk, McEntire, et al., 1997, 1997b, 1998; Williams & Mauk, 1997). However, we focus in the present paper on the study of electron PADs encountered in the large-scale magnetosphere of Jupiter rather than the local effect of a moon.

Mauk and Saur (2007) pursued the objective of identifying “magnetospheric” electron PADs observed by EPD in the 15–26 R_J region ($M \sim 15$ to $M \sim 70$), which may map to auroral regions. Their analysis relied on data accumulated at the maximum angular resolution of 64 sectors in order to look in detail for the beamness of field-aligned distributions to identify true auroral beams. Their analysis was therefore restricted to the E0 and E1 measurement channels (15–42 keV electrons, see Table 1).

Mauk and Saur (2007) found four types of 15–42 keV electron PADs in the 15–26 R_J region: pancake distributions, isotropic distributions, “scattered” field-aligned beams and “true” field-aligned beams. In their Figure 14, Mauk and Saur (2007) presented two spectra of true field-aligned beams for kinetic energies between 20 and 700 keV that show that auroral acceleration mechanisms may be a significant source of field-aligned electrons at kinetic energies of at least 700 keV. In the present article, we extend the conclusions of Mauk and Saur (2007) in the 15–26 R_J region to kinetic energies greater than 1 MeV, even if the angular resolutions of 32 sectors and 16 sectors available for the high energy channels (Table 1) are coarser than the 64-sector data product used in this previous work. We also investigate the PAD of energetic electrons at $M = 9$ where record-mode data are available.

2.1.5. Ulysses and Juno Observations of Energetic Electron PADs

During its 1992 fly-by of Jupiter, Ulysses observed from high latitudes quasi-periodic upward beams of >16 MeV electrons mapping to the outer magnetosphere (Simpson et al., 1992), showing that auroral acceleration mechanisms may accelerate electrons to 10s of MeV.

Onboard NASA's polar orbiting Juno, the Jupiter Energetic Detector Instrument (JEDI) (Mauk et al., 2017a) has been scrutinizing the spectrum and PAD of electrons with kinetic energies between 30 keV and 1 MeV since 2016. Juno-JEDI discovered the prevalence and persistence of upward electron beams on field lines connected to the main auroral ovals and polar cap of Jupiter (Allegrini, Mauk, et al., 2020; Mauk et al., 2017b, 2017c, 2020). Juno-JEDI also confirmed the Galileo result of Tomás et al. (2004) regarding the prevalence of field-aligned distributions near the magnetic equator in the $M > \sim 12$ region for <1 MeV electrons (Ma et al., 2021). However, previous Juno work did not investigate if these field-aligned distributions observed near the magnetic equator are scattered beams or true beams. Nevertheless, Juno-JEDI has clearly shown that high-latitude auroral acceleration mechanisms are able to accelerate electrons up to at least 1 MeV.

At higher kinetic energies, the omnidirectional flux of >10 MeV electrons inferred from noise in different systems onboard Juno has been frequently seen to increase when Juno was magnetically connected to Jupiter's aurora (Becker et al., 2017; Bonfond et al., 2018; Paranicas, Mauk, et al., 2018), and to increase or decrease when connected to the moons (Allegrini, Gladstone, et al., 2020; Connerney et al., 2020). Paranicas, Mauk, et al. (2018) presented a JEDI field-aligned electron PAD that may be dominated by 5–10 MeV electrons, but a definitive conclusion regarding the observed energy range could not be reached because JEDI was not designed to observe these electrons. Except in the latter case, the PAD of MeV electrons cannot be inferred from the indirect omnidirectional measurements, but the high-latitude passes of Juno and the comparison with <1 MeV JEDI data clearly hint that the aurora of Jupiter can accelerate electrons to tens of MeV.

The recent observations of Juno reinforce the hypothesis already proposed after the Ulysses fly-by that the acceleration mechanisms at work in the high-latitude aurora may be an important, if not dominant, source of keV, MeV and tens of MeV electrons trapped in the middle and outer magnetosphere of Jupiter. On this question, the observation of >1 MeV and >10 MeV PADs by Galileo-EPD can contribute to determine (a) if the intensity of the field-aligned beams of MeV electrons is sometimes greater than the flux of equatorial electrons, so that auroral electrons may be in sufficient number to contribute to the total content of energetic electrons, and (b) whether or not ‘scattered’ beams of MeV electrons exist, possibly showing that a mechanism scatters MeV field-aligned beams to populate the middle and outer magnetosphere with trapped MeV electrons.

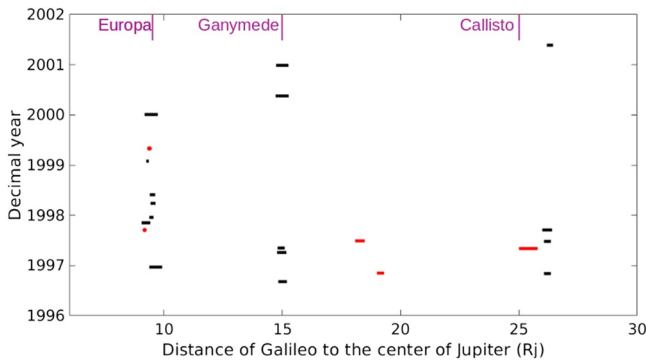


Figure 1. Time periods when Galileo-EPD accumulated record-mode observations of MeV electron fluxes. Periods in black include a close encounter with a moon, unlike periods in red. The x axis gives the radial distance of Galileo to the center of Jupiter.

In the next section, we present the time and space coverage of the considered record-mode dataset and the method employed to analyze the keV to >10 MeV electrons PADs collected by Galileo-EPD during these time periods.

3. Methods: Dataset, Record-Mode Coverage, and Analysis Approach

3.1. Galileo-EPD Electron Fluxes Corrected by Kollmann et al. (2019) and the Dataset of Miller et al. (2021)

The analysis presented in this article relies on the research-ready Galileo EPD and magnetic field dataset created by . (2021). This dataset has been submitted to NASA PDS and can be accessed at <https://github.com/fundamental-technologies-llc/galileo-issues-repository>.

The electron record-mode data that we use here were originally delivered to NASA's PDS PPI node. However, it is only recently that Kollmann et al. (2019) computed reliable EPD electron and ion fluxes corrected for instrument deadtime, background contamination, anomalous instrument

performance, and instrument degradation. The dataset created by Kollmann et al. (2019) has been submitted to NASA PDS and can be accessed at http://sd-www.jhuapl.edu/Galileo_EP/.

The Miller et al. (2021) dataset absorbs the particle fluxes corrected by Kollmann et al. (2019) and includes additional quantities, two of which have been key to the present analysis. First, the Miller dataset gives the running spin number of Galileo, which enabled to study electron PADs on a spin-by-spin basis as done in Mauk and Saur (2007) (see Section 3.3). Secondly, raw count rates of the DC2 and DC3 channels were provided in the Miller dataset and have been critical to estimate the background level and the counting statistics errors associated with the measurements collected by the two channels.

3.2. Record-Mode Time Periods Analyzed

Figure 1 shows the 21 record-mode periods when at least one of the three >1 MeV electron channels (B1, DC2, or DC3) collected reliable direction-resolved data in the 9–30 Rj region. Most record-mode periods of EPD were targeted to coincide with moon encounters, as is seen in Figure 1 in which time periods in black include a fly-by of Europa, Ganymede or Callisto. During the time intervals in red in Figure 1, >1 MeV electron direction-resolved data were accumulated far from any moon. The red periods therefore provide the best opportunities to identify the characteristics of magnetospheric electron PADs unperturbed by the immediate environment of the moons. In particular, the two orbital segments in 1996–310 and 1997–179 at 18 Rj and 19 Rj are totally unaffected by small-scale or large-scale effects associated to Galilean moons.

In this article, we do not analyze Galileo-EPD electron measurements collected inward of 9 Rj because they are unreliable (Kollmann et al., 2019). The present analysis focuses on record-mode periods collected at distances to the center of Jupiter lower than 30 Rj, because the counts accumulated during one 20-s Galileo spin drop to negligible level outward of this distance. Future work may try to accumulate direction-resolved data over several Galileo spins to advance on the question of the origin of MeV electrons in the outermost part of the Jovian magnetosphere (Kollmann et al., 2018). We therefore analyze the data gathered during 21 record-mode data periods at radial distances between 9 and 26 Rj following the approach detailed in the next section.

3.3. PAD Analysis Method

Several methods have been previously employed to analyze the PAD of energetic electrons and ions observed by the Galileo and Cassini orbiters at Jupiter and Saturn.

Firstly, each individual PAD collected during a spin of Galileo (~ 20 s) or a roll of Cassini (~ 23 – ~ 39 min) can be analyzed separately (Carbary et al., 2018; Mauk & Saur, 2007; Yuan et al., 2021), or PADs can be accumulated

over a longer period of time to increase the number of counts (Carbary et al., 2011; Clark et al., 2014; Kollmann et al., 2016; Nénon & André, 2019; Roussos et al., 2022; Tomás et al., 2004).

For Galileo, the advantage of working on a spin-by-spin basis is that the spatio-temporal variability of electron PAD can be resolved. In particular, Mauk and Saur (2007) have shown that 15–42 keV electron PADs substantially change on timescales sometimes as short as a Galileo spin, with an electron PAD for instance quickly changing from a strong field-aligned beam to an isotropic distribution. As we examine in the present paper the same region as Mauk and Saur (2007), we analyze energetic electron PADs spin by spin in order to investigate the spatio-temporal variability of MeV electron PADs. There are two main drawbacks to this approach which are carefully considered in the present analysis: (a) each Galileo spin generally provides a limited pitch angle coverage, and (b) the number of accumulated counts can be low, in particular far from Jupiter and for the high kinetic energy measurement channels. In the case of low counts, the Poisson counting statistics error may mask anisotropy amplitudes lower than the counting error. Nevertheless, the electron anisotropy is sometimes seen to be strong enough to reveal a clear PAD characteristic despite low counts (see Section 4).

Secondly, in order to report the shape of the PADs observed by Galileo, we may consider fitting the electron PADs with a functional form, as done in previous works at the giant planets (Clark et al., 2014; Mauk & Saur, 2007). However, we find that the limited number of data points per Galileo spin and the most-of-the-time narrow pitch angle range covered by EPD during one spin prevent from fitting the PAD shape with such a function. We instead performed the visual inspection of two kinds of plots: (a) individual PADs accumulated during each independent Galileo spin, and (b) one PAD time spectrogram for each record-mode period, that is, 21 spectrograms (see details two paragraphs below).

3.3.1. Estimating a Background Level

For the LET channels (E0-3, F0-3, and B1), a background level is computed based on the measurements collected when the EPD stepping motor was in position number 0, which placed the LET telescope behind a calibration shield. The HET end of LEMMS (DC2 and DC3 channels) was fully obscured in motor position number 5, where we compute the corresponding background level. We then require foreground count rates to be at least a factor of three above the estimated background level. Background is finally subtracted from the observed counts. Plots of the count rates observed by EPD as a function of time for each record-mode period are provided in an online repository (see Acknowledgments section).

3.3.2. Creating Individual Spin PAD Plots (One Per Galileo Spin) With 11 Subpanels (11 Electron Channels) Including Poisson Counting Error

The local pitch angle observed by the center of each detector field of view is computed thanks to the Galileo magnetometer observations integrated in the Miller et al. (2021) dataset that we use here. The M-shell parameter provided in the Miller dataset has been computed by Kollmann et al. (2019) using the internal magnetic field model VIP4 (Connerney et al., 1998) combined with the current sheet model of Khurana and Schwarzl (2005). We present in this article local pitch angles rather than equatorial pitch angles because the magnetic field model can be inaccurate in the middle and outer magnetosphere, and because we find that using equatorial pitch angle rather than local does not bring more information for the studied electron PADs (in particular, most local isotropic distributions are found to correspond to equatorial isotropic distributions and do not reflect the observation of a narrow range of equatorial pitch angles).

The HET end of EPD-LEMMS suffered from obscuration when the stepping motor was in positions number 3 to 7, so we follow the recommendation of Kollmann et al. (2019) to consider only HET data accumulated with motor positions equals to 0, 1, or 2.

For each individual Galileo spin with valid B1 (>1 MeV), DC2 (>1 MeV), or DC3 (>10 MeV) direction-resolved data, we plot the PAD observed by the 11 EPD electron channels (E0-E3, F0-F3, B1, DC2, and DC3 channels). These figures enable us to study whether the PAD morphologies observed at low and high energies are similar and may therefore be caused by a common physical mechanism. However, the comparison of all electron energies at a given time does not account for possible energy-time dispersed phenomena such as injections (see Section 5).

The example of an electron PAD accumulated at $M = 20.3$ is shown on Figure 2. The maximum resolution available for each channel is used (see Table 1, 64 sectors for E0 and E1, 32 sectors for E2-3 and F0-3, and 16 sectors for B1, DC2, and DC3). The vertical bars give the 1-sigma Poisson statistics counting errors, computed as \sqrt{N}/N

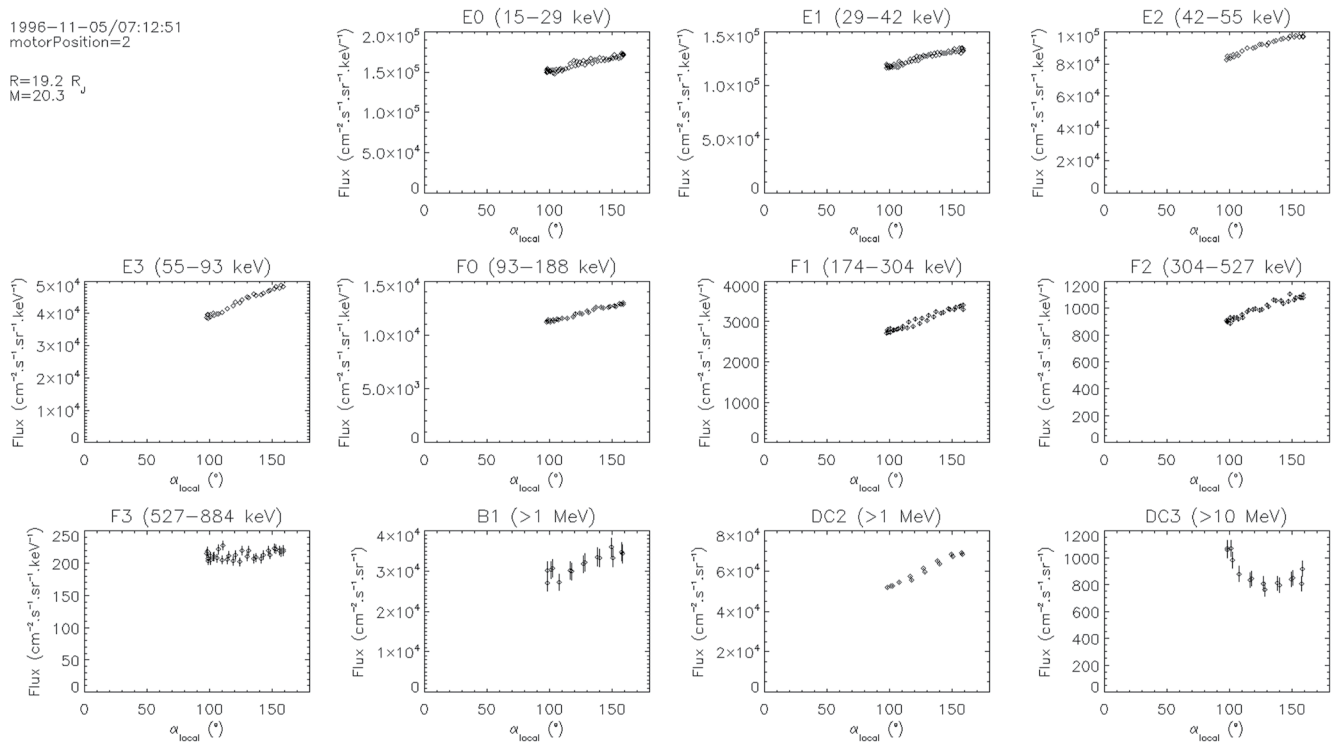


Figure 2. Energetic electron Pitch Angle Distribution observed during one Galileo 20-s spin in 1996-310. The listed UTC time indicates the beginning of the spacecraft spin. Error bars give the 1-sigma Poisson counting statistics error.

where N is the number of counts. A total of 3,064 individual plots have been created and visually inspected. These figures are provided in an online repository (see acknowledgments section).

3.3.3. Creating 21 PAD Spectrograms

In addition, for each of the 21 record-mode period, a spectrogram of electron PADs is created. Figure 3 shows the PAD spectrogram of energetic electrons observed by EPD during the 1996-310 orbital segment at $R = 19 R_J$ (no moon). For each Galileo spin, the PAD is normalized to the flux maximum. To analyze the PAD spectrograms, the reader is invited to look for the pitch angle position of green, blue, and black colors that indicate a reduced flux compared to the spin maximum flux. On the example spectrogram of Figure 3, one can clearly note that the DC2 and DC3 channels provided much less direction-resolved data than the other channels because of the HET end obscuration issue. In addition, one can note the persistence of field-aligned distributions (with a minimum near 90°) for the E0, E2, F1, B1, and DC2 channels. This feature is further discussed in Section 4.3.

While the time spectrograms enable us to easily visualize the temporal variability of electron PADs, we find that the individual spin plots most of the time give more information and details than the spectrograms alone. In particular, in the regions of low counts, the individual spin plots enable to appreciate if the anisotropy is larger than the counting errors. The analysis presented in the present paper relied mostly on the inspection of the individual spin plots.

Finally, for record-mode data collected during a close encounter with a moon, we use published simulations of the complex local electromagnetic environment of the moons to guide our analysis and extract as best as possible characteristics of magnetospheric electron PADs unperturbed by the local presence of the moon.

4. Results: Electron PADs Observed by Galileo-EPD From 9 R_J to 26 R_J

We present hereafter the shape of keV to >10 MeV electron PADs observed by Galileo-EPD during the 21 orbital segments when the instrument gathered record-mode data at $M \sim 9$, $M \sim 15$, $M \sim 20$ and $M \sim 26-60$ (see Section 3.2). We focus our analysis on instances when EPD most likely observed magnetospheric electron

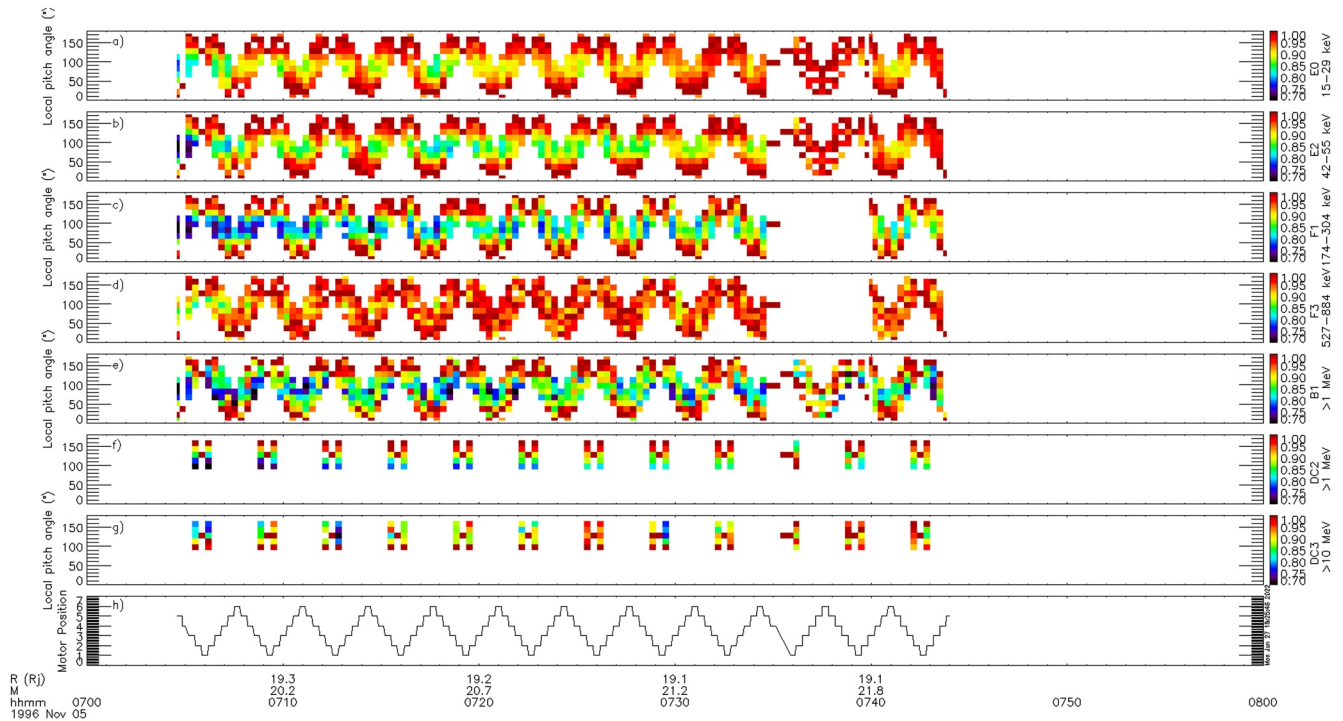


Figure 3. Electron Pitch Angle Distributions observed by Galileo-EPD in 1996-310 at a radial distance of 19.0–19.3 Rj. Fluxes are normalized to the maximum flux observed during each spacecraft spin. The measurement channel names and energy passbands are given on the right of the color bars. The label “R” gives the distance of Galileo to the center of Jupiter.

PADs rather than electron distributions locally perturbed by the nearby environment of the moons. The report is hereafter subdivided in sections organized by distance to Jupiter in order to determine if MeV electron PADs exhibit a radial transition similar to the one previously reported at lower kinetic energies with Galileo and Juno measurements (Tomás et al., 2004; Ma et al., 2021).

4.1. PAD of 20 keV to >10 MeV Electrons at $M \sim 9$

At $M \sim 9$, Galileo-EPD collected record-mode data during nine orbital segments. Two of those do not include a fly-by of Europa while the seven other segments include a close encounter with the icy moon during orbits E4, E11, E12, E14, E15, E19, and E26.

The observation of energetic electrons in the harsh radiation environment at $M = 9$ is challenging. Fluxes observed by the low energy channels of EPD have been strongly corrected for deadtime by Kollmann et al. (2019) because of the high foreground count rates. In addition, penetrating background is a major issue in this region. For the 10 orbital segments near $M \sim 9$, we have compared the foreground count rates with the background level (see Section 3.3.1). We find that the F0-3 measurement channels (93–884 keV electrons) are most of the time unreliable at $M \sim 9$ because the background rates are comparable to the foreground rates. On the other hand, we can most of the time proceed with the analysis of the measurements gathered by the E0-3 channels (15–93 keV) and B1, DC2, and DC3 channels (>1 MeV electrons).

The 10 PAD spectrograms near $M = 9$ (1 for each orbital segment) and the visual inspection of the individual spin PAD plots (see the online repository in the acknowledgments section) reveal that, clearly, <100 keV electrons and >1 MeV electrons always have a pancake PAD at $M \sim 9$.

We note the lack of field-aligned distributions or flux minima near 70° which could reveal an important effect of absorption by Europa, interaction with the neutral gas torus, or auroral acceleration, possibly showing that all these processes are of secondary order for energetic electrons at $M \sim 9$. In addition, the lack of isotropic distributions indicates that electron pitch angle scattering at $M \sim 9$ is below the strong diffusion limit.

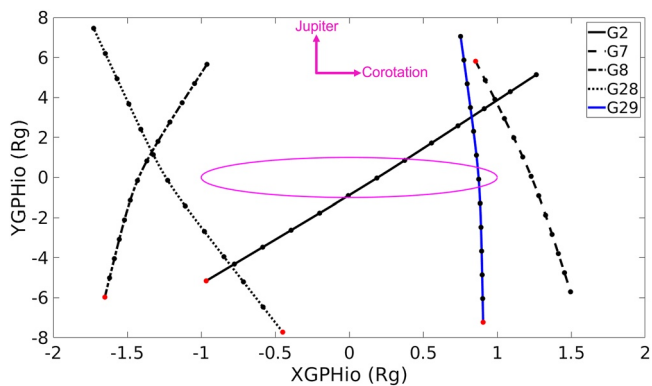


Figure 4. The trajectory of Galileo in GPhiO coordinates during the five considered encounters with Ganymede ($1 R_g = 2,634 \text{ km}$). Ganymede's radius is shown with the purple circle. The red dots give the position of Galileo at the beginning of each time period, tick marks give Galileo's position every 5 min. The red dots are at 18:30, 06:40, 15:25, 09:40, and 07:55 UTC for G2, G7, G8, G28, and G29, respectively.

4.2. At $R = 15 R_j$, $M \sim 15\text{--}18$

At $R = 15 R_j$, all EPD record mode data were acquired during close encounters with Ganymede, specifically during orbits G2, G7, G8, G28, and G29. Figure 4 shows the trajectory of Galileo projected in the X-Y plane of the GPhiO coordinate frame, where +X points along the corotation direction (hence Galileo was upstream of Ganymede at $X < 0$) and +Y points toward Jupiter (position data were retrieved on NASA's PDS PPI). It can be seen that Galileo remained upstream of Ganymede during the G8 and G28 encounters, downstream of the moon during G7 and G29, while the G2 encounter is an upstream-downstream pass over the north pole of Ganymede. The terms "upstream" and "downstream" refer here to the cold plasma flow. However, electrons with a kinetic energy greater than a few MeV can drift in the direction opposite to the Ganymede velocity from the downstream to the upstream hemispheres of Ganymede (Liuzzo et al., 2020). An immediate local effect of Ganymede would therefore be seen downstream of the moon for electrons with kinetic energies lower than a few MeV but upstream of Ganymede for higher energy electrons. However, the reversal energy of a few MeV may depend on the considered Jovian magnetic field model, on the assumed corotation rate, and on the electron pitch angle.

The knowledge of Galileo's position in GPhiO coordinates is not sufficient to figure out if the spacecraft was on Jovian magnetic field lines unperturbed by the environment of Ganymede and connected on their two ends to the giant planet ionosphere. To identify the time periods when Galileo was on such field lines and when EPD could therefore reveal magnetospheric PADs, we use the field line tracing results shown on Figure 1 of Kivelson et al. (1998) for the G2, G7, and G8 encounters, Figure 4 of Kivelson et al. (2002) for G28 and Figure 4 of Williams (2004) for G29.

During the five orbital segments at $M \sim 15\text{--}18$, foreground count rates dominate by a factor of 5–10 over the estimated background when Galileo was outside of the magnetosphere of Ganymede. In addition, the observed count rates were below saturation level for all the considered electron channels. We therefore proceed with the analysis of the electron PADs at $M \sim 15\text{--}18$.

Mauk and Saur (2007) analyzed the magnetospheric PADs of 15–42 keV electrons (E0 and E1 channels) observed by EPD during the G28 encounter. Here, we extend the previous analysis to four additional passes and to higher kinetic energies, up to $>10 \text{ MeV}$. The identification of the most favorable time periods to study magnetospheric PADs and the detailed analysis of the EPD data gathered during each fly-by are given in Supporting Information S1. Table 2 presents the shape of electron PADs observed by Galileo-EPD at $M \sim 15\text{--}18$.

In Table 2, text in bold shows the PAD observations that are most likely to reveal PADs of electrons in the undisturbed Jovian environment because a local effect of Ganymede on electron distributions would propagate downstream of the moon for $<1 \text{ MeV}$ electrons (E and F channels) and upstream of it for electrons with kinetic energies greater than a few MeV (B1, DC2, DC3) (Liuzzo et al., 2020). An exception is G8 where PADs may have all been accumulated too close to Ganymede (see Supporting Information S1). The B1 and DC2 integral channels observed $>1 \text{ MeV}$ electrons, so the influence of Ganymede on the PADs observed by these channels may be seen either upstream or downstream of the moon depending on whether the observed electron counts are dominated by $\sim 1 \text{ MeV}$ electrons or by multi-MeV electrons.

For 15–42 keV electrons (E0 and E1 channels) in the Jovian environment at $M \sim 15$, we confirm with G2 data the prevalence of isotropic and scattered beam distributions previously reported by Mauk and Saur (2007) with G28 measurements. However, contrary to G28 observations, we do not find any evidence of true beam distribution during G2. The process which creates keV true beams, possibly auroral acceleration mechanisms, therefore appears to be transient in time or space.

The true beams and scattered beam distributions observed by the lowest energy channels are sometimes but not always seen to extend to kinetic energies of 100s of keV. The scattered beams observed for MeV electrons do not resemble their lower energy counterparts, so we did not find any evidence that true auroral beams influence MeV electron distributions at $M \sim 15$.

Table 2

Summary of Magnetospheric Electron PADs Observed by Galileo-EPD at $M \sim 15$ as far as Possible From the Local Environment of Ganymede

Record-mode period	Upstream for E and F channels (20–700 keV)	Upstream for B1 and DC channels (>1 MeV)	Downstream for E and F channels (20–700 keV)	Downstream for B1 and DC channels (>1 MeV)
G8 (1997-127, all the record-mode period may be locally influenced by Ganymede)	Butterflies	B1: butterflies DC2 and DC3 (pitch angle coverage mostly around the perpendicular direction): scattered beams which may be the central part of butterflies		
G28 (2000-141)	True beams and scattered beams up to a variable upper energy, above which isotropic distributions	Scattered beams at the beginning of the fly-by, superposition of pancake + scattered beam at the end (the scattered beams may show losses of equatorial electrons)		
G2 (1996-250)	E: scattered beams, no true beams F: isotropic	B1: isotropic distributions and scattered beams DC2: isotropic DC3: scattered beams	E: scattered beams, no true beams F: isotropic	B1: no data DC2 and DC3: isotropic distributions and pancakes
G7 (1997-095)			Butterflies	B1: butterflies DC2 and DC3: maybe isotropic, scattered beam or butterfly
G29 (2000-363)			Scattered beams and butterflies, scattered beams are stronger at F energies compared to E	B1: butterflies and scattered beams DC2 and DC3: isotropic distributions and pancakes

Note. Text in bold gives the PADs which are most likely characteristics of Jovian electrons rather than signatures of the local influence of the moon.

Given the limited number and extent of EPD data at $M = 15$, we cannot firmly conclude if the scattered beams and butterfly distributions observed for MeV electrons reveal signatures of the Ganymede environment or characteristics of the Jovian environment (see detailed discussion for each Ganymede encounter in Supporting Information S1). However, the EPD data show isotropic and pancake distributions that we believe likely are characteristics of MeV electron distributions at $M \sim 15$. It is therefore possible that the PAD of MeV electrons not locally perturbed by Ganymede would mostly consist of isotropic and pancake distributions.

Future work may analyze <1 MeV electron PADs collected by Juno at $M \sim 15$ far from Ganymede to identify whether the scattered beams and butterfly distributions observed by Galileo-EPD are a characteristic of magnetospheric electrons or a local influence of Ganymede. Future observations of keV to several tens of MeV electrons by the Particle Environment Package (PEP) and RADiation hard Electron Monitor (RADEM) of ESA's JUICE mission, far from and close to Ganymede, will also help to advance on this open question (see Section 5.1) (Grasset et al., 2013).

4.3. At $R \sim 18\text{--}19 R_j$, $M \sim 20\text{--}25$

During two orbital segments in 1996-310 and 1997-179, Galileo-EPD collected record-mode data at radial distances of $\sim 18\text{--}19 R_j$ (Figure 1) mapping to $M \sim 20\text{--}25$. These measurements were therefore collected far from the drift shells intercepted by Ganymede ($M = 15\text{--}18$) and Callisto ($M = 26\text{--}70$) (Paranicas, Mauk, et al., 2018), and thus reveal characteristics of the magnetosphere unaltered by the presence of a moon. We describe in detail the electron PADs observed during the two orbital segments, and Table 3 then sums up our conclusions at this radial distance.

Table 3

Energetic Electron PADs Observed by Galileo-EPD at $R = 18\text{--}19 R_j$

Record-mode period	Electron PADs observed by the E and F channels (20–700 keV)	Electron PADs observed by the B1, DC2, and DC3 channels (>1 MeV)
1996–310 $R = 19.0\text{--}19.3 R_j$ $M = 20.0\text{--}22.1$ Local Time = 21 hr	Persistent scattered beams at the beginning of the period, persistent isotropic distributions after	B1 and DC2: persistent scattered beams DC3: persistent overlap of a field-aligned component on top of a pancake (see Figure 5)
1997–179 $R = 18.1\text{--}18.5 R_j$ $M = 19.9\text{--}24.9$ Local Time = 06 hr	True beams, scattered beams, and isotropic distributions	DC2: isotropic B1 and DC3: large counting errors

Note. The term “large counting errors” means that the observed anisotropy was smaller than the counting errors.

4.3.1. 1996–310, $R = 19.0\text{--}19.3 R_j$, $M = 20.0\text{--}22.1$, Local Time = 21 hr

In 1996-310, Figure 3h shows that the LET end of EPD-LEMMS was never placed behind the calibration shield (motor position 0), hence the background levels for the E, F, and B1 electron channels were not measured. However, we use the measurements collected in 1997-179 at a similar radial distance (see next subsection) to estimate the signal-to-noise ratio (SNR) of these channels in 1996-310. Specifically, we linearly scale the background levels observed in 1997-179 with the B1, DC2, and DC3 count rates observed at the two dates, as the MeV electron observations give an indication about the penetrating environment. In 1997-170, the MeV radiation environment had an intensity lower than in 1996-310 by a factor of ~ 3 . We can therefore compute that, in 1996-310, the F3 channel had a background level of ~ 30 counts per second, while the measured signal was of 1,000 counts per second (signal-to-noise ratio, SNR, of 30). This way, we find that the E, F, and B1 channels all have SNRs larger than 10 in 1996-310 and we proceed with the analysis of the LET channels data. For the DC2 and DC3 observations collected by the HET end, background measurements gathered during maximum obscuration of the field of view (motor position 5) show that foreground count rates are a factor of 6 above background level.

This time period was not analyzed by Mauk and Saur (2007). Figure 3a shows that 20 keV electrons present field-aligned distributions at the beginning of the time period that gradually seem to disappear as Galileo goes from $M = 20.0$ to $M = 22.1$. For the E2 and F1 channels (48–200 keV, Figures 3b and 3c), field-aligned distributions may have persisted during the entire time period. Our visual inspection of individual spin plots shows a similar behavior for 400 keV F2 PADs, whereas the 700 keV F3 data (Figure 3d) appears mostly isotropic, except at the very beginning of the time period.

The B1 and DC2 channels (>1 MeV electrons) both clearly show field-aligned distributions which persisted during the entire record-mode data period, except maybe during one Galileo spin at 07:36. However, the persistent >1 MeV electron field-aligned distributions are not clearly seen at DC3 >10 MeV energies (Figure 3g). The DC3 channel instead mostly shows pancake distributions (e.g., at 07:05–07:06, 07:09, 07:12, 07:15–16) and a second type of PADs with two flux maxima at pitch angles near 90° and 180° (e.g., at 07:12, 07:15, 07:19, 07:25, 07:29, 07:32, 07:42). The DC3 >10 MeV PADs with two maxima are further investigated with Figure 5 which shows selected electron PADs throughout the 1996-310 record-mode period. The >10 MeV PADs seem to repeatedly show a field-aligned component superimposed on a pancake distribution.

The modest field-aligned distributions at the lowest energies which seem to be more anisotropic with increasing energy up to 400 keV, appear isotropic at 700 keV and are finally strongly field-aligned for >1 MeV electrons are challenging to explain. For MeV electron PADs, a possible interpretation of the B1, DC2, and DC3 observations is that a physical process generates MeV scattered beams with flux intensities which decrease with increasing kinetic energy. For >1 MeV electrons, the scattered beam intensity may be greater than the background isotropic or pancake distribution at most pitch angles, hence the PAD appears field-aligned. For >10 MeV electrons, the net superposition of a pancake distribution and of a scattered beam may lead to the observed distribution if the scattered beam intensity is greater than the pancake fluxes only in the field-aligned directions.

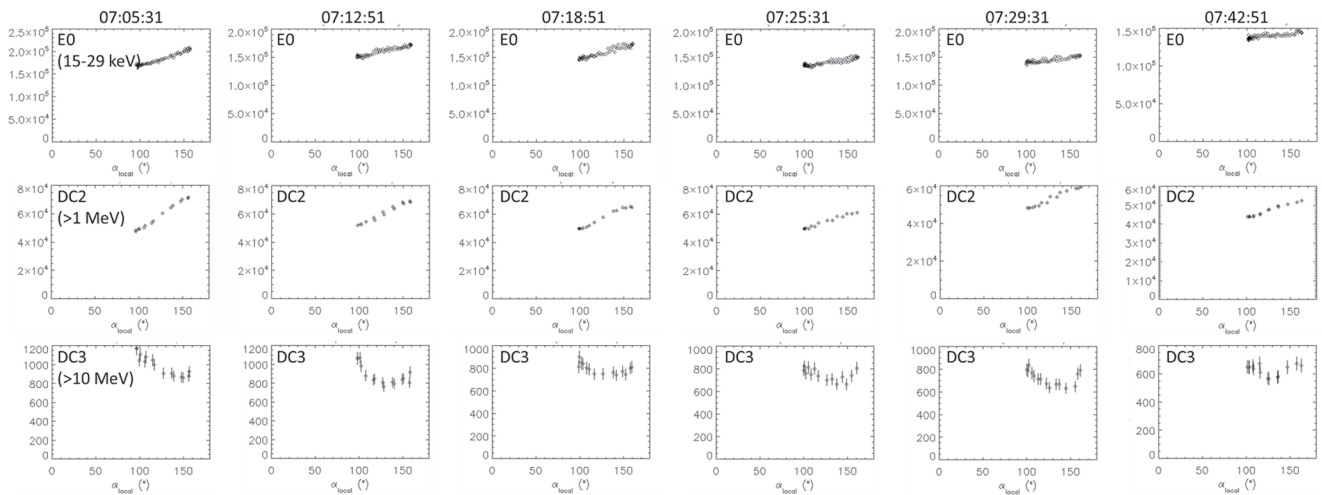


Figure 5. Electron PADs observed at selected times in 1996–310. E0 observed 15–29 keV electrons, DC2 >1 MeV electrons and DC3 >10 MeV electrons. Flux units are $\text{cm}^{-2}\cdot\text{s}^{-1}\cdot\text{sr}^{-1}\cdot\text{keV}^{-1}$ for E0 and $\text{cm}^{-2}\cdot\text{s}^{-1}\cdot\text{sr}^{-1}$ for the DC2 and DC3 integral channels.

4.3.2. 1997–179, $R = 18.1\text{--}18.5$, $M = 19.9\text{--}24.9$, Local Time = 06 hr

Mauk and Saur (2007) analyzed the 64-sector data accumulated by the E0 and E1 channels (15–42 keV electrons) in 1997–179 and found intense true beams and scattered beams which quickly alternate with fully isotropic distributions. Here, we extend this previous work to higher kinetic energies.

Foreground count rates were a factor of more than 3 above the background level for all measurement channels. As can be seen in the individual PAD plots provided in the online repository (see acknowledgments section), some of the intense true beams documented by Mauk and Saur (2007) extend to kinetic energies of 700 keV (e.g., at 14:09, 14:11, 14:13, 14:25, 14:28), while others do not (e.g., 13:55, 13:57). The mechanism responsible for the true beams therefore not only shows a spatio/temporal variability but also exhibits a variable energetics.

DC2 measurements remained isotropic during the entire period of 1997–179, which contrasts with the DC2 field-aligned PADs observed at a similar radial distance in 1996–310. For the B1 and DC3 channels, the counts accumulated during each integration time in 1997–179 were relatively low, leading to Poisson counting statistics errors greater than 30%. Our visual inspection of B1 and DC3 PADS spin by spin did not enable us to find any anisotropy for B1 and DC3 larger than the counting errors.

4.3.3. Summary of Electrons PADs Observed at $R \sim 18\text{--}19$ Rj, $M = 20\text{--}25$

Table 3 sums up our conclusions regarding the electron PADs observed by the record acquisition mode of Galileo-EPD at radial distances of 18–19 Rj which may map to $M \sim 20\text{--}25$. This is well outside the range where particles may encounter Ganymede or Callisto during their drift (Paranicas, Mauk, et al., 2018). We find that the true beams observed in 1997–179 and reported by Mauk and Saur (2007) have not been observed in 1996–310. We also find persistent MeV electron scattered beam PADs that have been observed in 1996–310 but not in 1997–129. The physical mechanism which creates the MeV field-aligned distributions may therefore be variable in time or have a local time dependency.

4.4. At $R \sim 26$ Rj, $M = 25\text{--}60$

Galileo-EPD collected MeV electron PADs during 5 time periods at a radial distance around 26 Rj (Figure 1). In 1997–126, Galileo remained at distances larger than 0.5 Rj from Callisto, while the four other time periods include a close encounter with Callisto (C3, C9, C10, and C30 encounters). Table 4 presents the shape of energetic electron PADs observed by Galileo-EPD, and a detailed analysis of magnetospheric record-mode data for each independent period of time is provided in Supporting Information S1.

Table 4

Summary of Energetic Electron PADs Observed by the Record Acquisition Mode of Galileo-EPD at $R \sim 26 R_J$

Orbital segment	Electron PADs observed by the E and F channels (20–700 keV)	Electron PADs observed by the B1, DC2, and DC3 channels (>1 MeV)
1997-126 (no moon encounter); $M = 25\text{--}57$	Isotropic, pancakes, scattered beams, true beams	B1: large counting errors DC2 and DC3: isotropic and pancakes
1997-176 (C9 encounter); $M = 52\text{--}60$	Isotropic, pancakes, scattered beams, true beams	B1: large counting errors DC2 and DC3: isotropic and pancakes + one field-aligned distribution superposed on a pancake observed only during one Galileo spin in B1, DC2, and DC3 data at 14:09
1996-309 (C3 encounter); $M = 46\text{--}53$	Isotropic outside of Callisto's wake, beams in the wake	DC2: isotropic outside of the wake B1 and DC3: large counting errors outside of the wake. >1 MeV electron PADs show field-aligned distributions in the wake (may be a local effect of Callisto)
1997-259 (C10 encounter); $M = 29\text{--}54$	Isotropic and scattered beam distributions, no true beam	DC2: isotropic B1 and DC3: large counting errors
2001-145 (C30 encounter); $M = 35\text{--}42$	Isotropic, pancakes, scattered beams, true beams	DC2: isotropic DC3: large counting errors B1: large counting errors except during 4 spins

Four Galileo spins show field-aligned distributions at E, F, and B1 energies (see Figure 6)

Note. "Large counting errors" means that the observed anisotropy was lower than the counting error. Text in bold highlights magnetospheric MeV electron PADs.

For 15–42 keV electrons, Mauk and Saur (2007) identified true 'auroral' electron beams in 1996-126 (no fly-by) and during the C3 and C9 encounters, and we find another case during C30. C10 on the other hand did not show any true beam.

Text in bold in Table 4 highlights MeV electron PADs that may be characteristics of the Jovian magnetosphere and shows that, most of the time, isotropic and pancake distributions were observed for MeV electrons. One 20-s Galileo spin during C9 shows a possibly-magnetospheric field-aligned electron distribution superimposed on a pancake distribution.

During the C30 record-mode period in 2001-145, 11 Galileo spins provided MeV electron direction-resolved observations that covered field-aligned directions and were accumulated far from Callisto (distance larger than 0.1 R_J from the center of the moon). Out of these 11 spins, 4 spins reveal MeV electron field-aligned distributions observed by the B1 channel, both at the beginning and end of the record-mode period. It is therefore possible that the B1 MeV electron field-aligned distributions persisted during the 30 min of the C30 record-mode period. DC2 and DC3 data were not available during these particular spins. The four C30 Galileo spins of interest, shown on Figure 6, are likely unrelated to an immediate effect of Callisto (see Supporting Information S1).

At 11:09 during C30 (Figure 6, left column), a very intense true beam is observed at all electron energies from 20 keV to >1 MeV, superimposed on a pancake distribution. At 11:10, B1 (>1 MeV electrons) shows a clear scattered beam component possibly superimposed on a pancake. The F2 channel may show a similar feature, but the lowest energy channel E0 does not exhibit a clear field-aligned distribution, so the MeV electron field-aligned component seems unrelated to the keV electron distribution. At 11:42, two successive Galileo spins (two right columns of Figure 6) also show B1 and F2 scattered beams. The shape of low-energy PADs observed during these two spins does not resemble higher-energy field-aligned distributions, so it is hard to conclude if a common mechanism is responsible at this time for the PAD of 10s of keV electrons, 100s of keV electrons, and MeV electrons.

The origin of the persistent MeV electron field-aligned distributions can be high-latitude auroral acceleration, outward adiabatic transport or absorption by Callisto (a large-scale macro signature or a drifting micro signature). The sparse and limited dataset collected by Galileo-EPD is sufficient to detect for the first time this transient characteristic of MeV electrons at 26 R_J but is too limited to firmly establish the origin of the MeV electron field-aligned components.

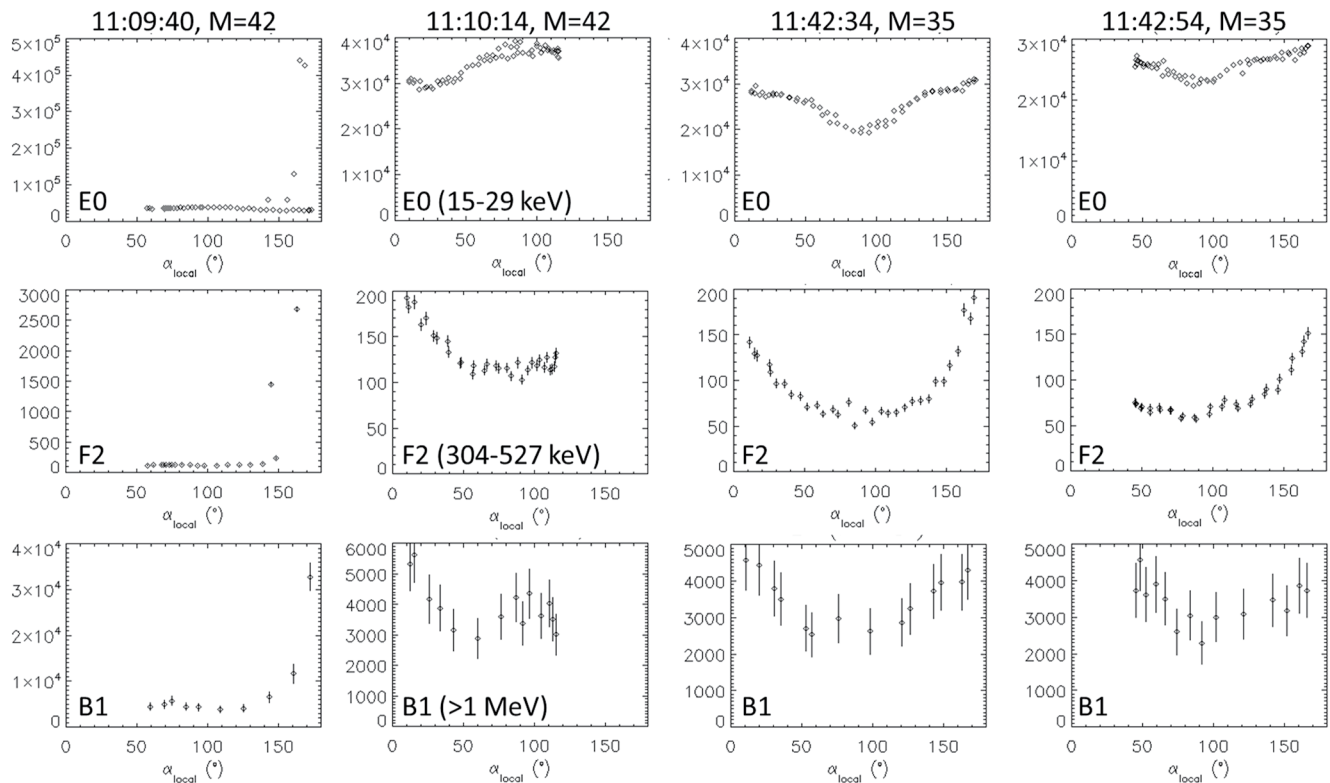


Figure 6. Energetic electron PADs observed by Galileo-EPD during 4 selected spacecraft spins far from Callisto during the C30 encounter. E0 observed 15–29 keV electrons, F2 observed 304–522 keV electrons, and B1 >1 MeV electrons. Flux units are $\text{cm}^{-2}\cdot\text{s}^{-1}\cdot\text{sr}^{-1}\cdot\text{keV}^{-1}$ for E0 and F2 and $\text{cm}^{-2}\cdot\text{s}^{-1}\cdot\text{sr}^{-1}$ for the B1 integral channel.

5. Summary, Conclusions, and Discussions

The EPD experiment onboard NASA's Galileo mission observed from 1995 to 2003 the PAD of 20 keV to >10 MeV electrons in the magnetosphere of Jupiter. MeV electron PADs were accumulated only when the high cadence acquisition mode of the instrument (known as the “record mode”) was activated, that is, during short 1–2 hr time intervals. Specifically, MeV electron PADs have been collected at radial distances of 9 R_j ($M \sim 9$), 15 R_j ($M \sim 15$ –18), 18–19 R_j ($M \sim 20$ –25), and 26 R_j ($M \sim 26$ –60). The collected dataset of MeV electron PADs has therefore a limited temporal and spatial coverage, yet it remains unprecedented because Galileo-EPD is the only experiment ever designed to observe the anisotropy of MeV electrons at Jupiter. In this article, the first analysis of MeV electron PADs observed by Galileo-EPD has been presented.

The present study focused on the shape of energetic electron PADs in the magnetosphere of Jupiter. During close encounters with Europa, Ganymede, or Callisto, a particular attention has been put forth to try to disentangle as best as possible the local influence of the moon environments on electron distributions from the magnetospheric PADs that this article focuses on.

Despite the fact that our analysis relied on an extremely sparse dataset, clear characteristics of MeV electron PADs are identified. Figure 7 summarizes the PAD shapes observed for MeV electrons during the record-mode type periods. We detail hereafter the implication of the observed PADs on our understanding of MeV electrons in the magnetosphere of Jupiter.

1. The MeV electron PADs observed by Galileo-EPD are relatively isotropic from $M = 9$ to $M = 60$, with the peak-to-peak flux anisotropy being lower than 3 when EPD scanned different pitch angles. However, the angular apertures of 15° and 45° of the EPD telescopes may smooth sharp electron gradients. In particular, the atmospheric loss cone is not resolved by EPD.

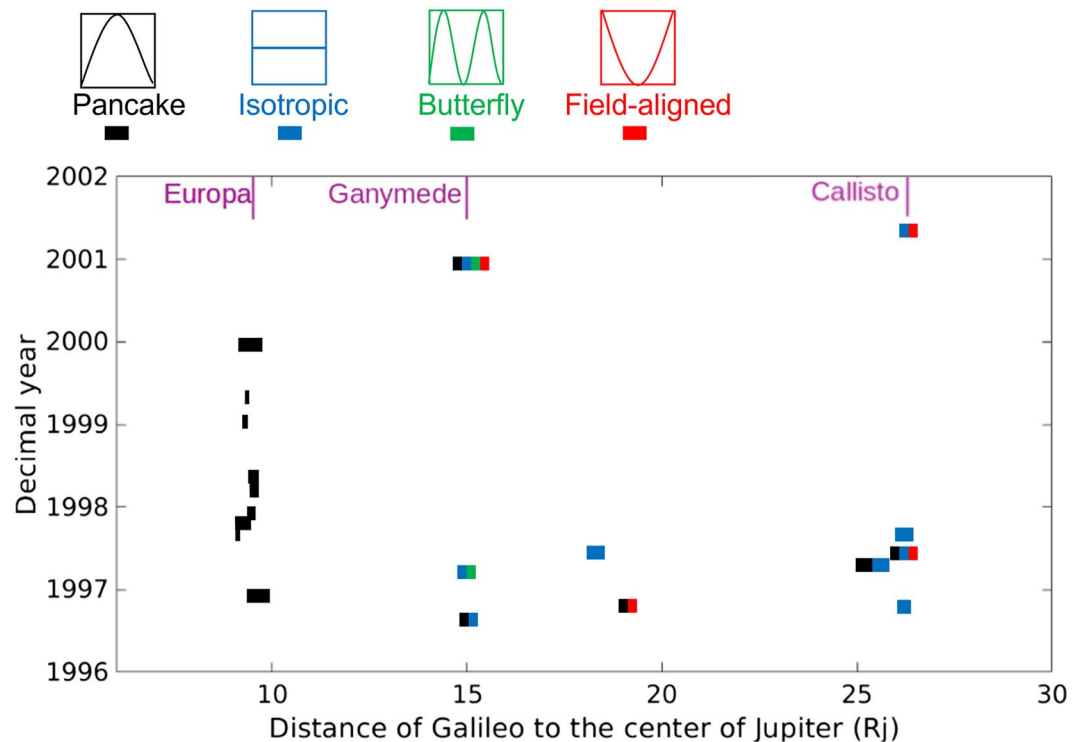


Figure 7. Summary of the shape of PADs observed for MeV electrons by Galileo. Outward of 14 Rj, PAD shapes are dynamic and can change on a timescale as short as 20 s. The colors shown here do not show the PAD shapes along orbital trajectories, but display the shape of PADs observed during each record-mode time period.

We therefore confirm the assumption of quasi-isotropy used in previous work which relied on omnidirectional flux measurements to infer the flux and phase space density of equatorial electrons (with an equatorial pitch angle of 90°) (Garrett & Jun 2021; Kollmann et al., 2018).

We also confirm the isotropy assumption used in previous work which computed electron precipitation patterns on moon surfaces (e.g., Liuzzo et al., 2015, 2017, 2019, 2020; Nordheim et al., 2018). However, the relatively large aperture of the EPD telescopes may smooth out the beamness of the keV to MeV field-aligned beams encountered by Ganymede and Callisto (Mauk & Saur, 2007). Future work may investigate the effect of transient field-aligned beams of electrons on the bombardment and weathering of the two icy moon surfaces. We however note that the Galileo sparse dataset does not constrain the occurrence rate of field-aligned bursts bombarding the moons near the magnetic equator, something which can be investigated with Juno data in the <1 MeV energy range.

For the assessment of radiation hazard, the quasi-isotropic characteristic of MeV electron fluxes implies that a direction-resolved flux taken in any direction of the sky would likely inform on the harmful *omnidirectional* flux. This conclusion is of particular interest for future radiation monitor observations that may observe particles coming from a narrow solid angle. For instance, the radiation monitor onboard ESA's JUICE mission will observe MeV electrons in a field of view covering only 1% of the sky (Pinto et al., 2020; Socha, 2021; Socha et al., 2020).

2. At $M \sim 9$, electrons with kinetic energies lower than 100 keV or greater than 1 MeV always have a pancake PAD. Measurement channels with energies in between are most of the time unreliable at 9 Rj.

The pancake PADs at 9 Rj may be the signature of adiabatic inward radial transport, local acceleration of equatorial electrons by wave-particle interaction, or local pitch angle scattering (Li et al., 2016; Ma et al., 2020). The electron distributions are in particular not isotropic at $M = 9$, meaning that the scattering of energetic electrons by electromagnetic waves at work at $M \sim 9-10$ (Li et al., 2021) does not reach the strong diffusion limit. We also do not find any evidence for a large-scale absorption effect of Europa on MeV electron distributions.

3. Pancake distributions are observed at all radial distances from 9 R_j to 26 R_j ($M = 9$ to $M = 60$), even if it is not the dominant PAD observed outward of 15 R_j.

The simplest explanation of the existence of these pancake PADs in this large range of M-shell is that adiabatic radial transport is at work in most of the magnetosphere of Jupiter, as proposed by Kollmann et al. (2018) for $M > 20$ based on Galileo-EPD omnidirectional spectra.

4. Isotropic distributions for 20 keV to >10 MeV electrons are often seen at 15 R_j, 19–20 R_j, and 26 R_j.

In this work, electron PADs were analyzed using the local pitch angle rather than the equatorial one (see Section 3.3). We find that most of the locally isotropic distributions actually correspond to equatorial isotropic distributions if we were to convert local pitch angles to equatorial ones.

Future work should investigate the origin of these isotropic distributions. Equatorial magnetic field curvature scattering is an unlikely candidate, but advanced numerical tracing of electron trajectories is needed to confirm this statement (e.g., Achilleos et al., 2021). Pitch angle scattering by resonant interaction with electromagnetic waves may explain the existence of isotropic distributions, but future work is needed to investigate if wave mode and intensities able to scatter electrons over such a broad range of energies exist. We note that, similarly, the origin of energetic electron isotropic distributions in the outer magnetosphere of Saturn remains a mystery (Clark et al., 2014).

5. Scattered field-aligned distributions and butterfly distributions are observed for 20 keV to >10 MeV electron PADs close to Ganymede at $M \sim 15$.

We cannot firmly conclude if these distributions reveal local perturbations of Ganymede on electron distributions or if they show transient characteristics of the Jovian magnetosphere at $M \sim 15$. Juno observations can be used to further investigate this topic in the <1 MeV energy range.

6. At $R = 19$ –20 R_j, MeV electron scattered field-aligned distributions have been observed to persist during the one-hour period of high-resolution measurements accumulated in 1996–310 ($M = 20$ –22, Local Time = 21 hr). However, in 1997–179 ($M = 20$ –25, Local Time = 06 hr), no such field-aligned distribution was detected.

The 1996–310 field-aligned distributions may be evidence of two distinct phenomena that cannot be distinguished with the limited Galileo-EPD dataset.

First, the field-aligned distributions may be evidence that high-latitude auroral acceleration mechanisms supply the middle magnetosphere with trapped MeV electrons. In this case, the Galileo detection of scattered field-aligned distributions at 19 R_j would be a proof that the field-aligned bursts of keV to >10 MeV electrons detected by Ulysses and Juno at high latitude (Becker et al., 2017; Bonfond et al., 2018; Paranicas, Mauk, et al., 2018; Simpson et al., 1992) can be scattered to populate the magnetosphere with trapped particles.

A second hypothesis is that the observed distributions reveal that outward adiabatic transport is at work, at least transiently, in the middle magnetosphere. The latter outward transport can result from radial diffusion if the PSD radial profile has a negative slope (PSD decreasing with L), or can be caused by the possible large-scale convective dawn-to-dusk electric field.

The field-aligned distributions were not observed in 1997–170 at a similar radial distance, showing that the underlying process is either time or local time dependent.

7. At $R = 26$ R_j, field-aligned scattered beam distributions have been identified in MeV electron data far from Callisto for 2 of the 6 considered passes, namely during the C9 encounter (1997–176, $M \sim 50$) and during the C30 encounter (2001–145, $M \sim 40$).

As discussed in Section 4.4, these field-aligned PADs are unlikely the result of a local effect of Callisto. They may reveal a large-scale macro-signature of Callisto on the drift shells intercepted by the Galilean moon, a drifting micro-signature echo of Callisto absorption, outward adiabatic transport, or they can be an evidence of MeV auroral beams at Callisto's distance.

8. The shape of the field-aligned distributions detected for MeV electrons at $R = 15$ R_j, $R = 18$ –19 R_j, and $R = 26$ R_j, does not resemble the shape of lower energy distributions. The energy dependency of electron PAD shapes may be leveraged in future work and with future measurements to investigate the origin of the observed PADs.

9. MeV electron PADs exhibit a transition from stable pancake distributions at $R = 9 R_J$ to variable and diverse PAD shapes outward of $15 R_J$. A similar transition has been previously reported in the Jovian magnetosphere for keV to hundreds of keV electrons based on Galileo and Juno measurements (Tomás et al., 2004; Ma et al., 2021), and for keV to tens of MeV electrons at Saturn (e.g., Clark et al., 2014).

The electron PAD may also be studied in concomitance with the particle energy spectrum, as both fundamental properties of the electron distribution are powerful indicators of the physical processes at work (Kollmann et al., 2018). *Direction-averaged* energy spectra enable to study if spectra substantially change when electron PADs vary. Furthermore, *direction-resolved* energy spectra would enable to constrain the energy spectra of the pancake and field-aligned components of the electron distributions in order to investigate if they reveal distinct sources of energetic electrons. However, the F channels that observed 93–884 keV electrons are unreliable at $M \sim 9$ and provide limited counts during a 20-s Galileo spin at $M > 15$. These limitations prevent us from computing the aforementioned direction-averaged and direction-resolved spectra, as done with 11-min EPD omnidirectional measurements by Kollmann et al. (2018).

We also acknowledge that electron PADs have been studied in this article without considering the dynamics of the magnetosphere. In particular, injection events may transiently create pancake PADs which would be detected at the spacecraft location with an energy-drift dependent timing.

Finally, the occurrence rate of the different PAD shapes as a function of L and local time could not be constrained with the limited Galileo-EPD record-mode dataset. Using Juno < 1 MeV electron data, Ma et al. (2021) computed the long-term average of electron PADs, but future work may consider the investigation of the occurrence rate of the different kind of PADs (isotropic, pancake, butterfly, scattered beam, true beam), as done by Clark et al. (2014) at Saturn.

5.1. Future Observations of MeV Electron PADs in the Jovian Magnetosphere

Understanding the origin and dynamics of > 1 MeV electrons at Jupiter is critical to our understanding of magnetospheres and particle acceleration in the solar system and beyond. The first step toward this objective is the accumulation of reliable electron spectra and PADs. Here, we have presented the first analysis of the dataset of MeV electrons PADs collected by Galileo-EPD. However, the dataset is very sparse in space and time. In addition, MeV electrons were observed only by three integral channels that may mix up different electron energy ranges. Finally, the EPD telescopes had relatively large opening angles of 15° and 45° that could not resolve the loss cone at the equator and may have smoothed out field-aligned beams.

After 2031, the radiation monitor RADEM (Radiation-hard Electron Monitor) onboard ESA's JUICE mission will observe the direction-resolved flux of 100s of keV to 10s of MeV electrons in the Jovian magnetosphere (e.g., Pinto et al., 2020; Socha, 2021; Socha et al., 2020). Two subsystems of RADEM will monitor energetic electrons: (a) the Directional Detector Head (JUICE-RADEM-DDH) will observe ~ 300 keV–2 MeV electrons (one integral channel) and is designed to finely study their anisotropy by observing electron flux in angular sectors which will have an opening angle of 7° and will cover close to half of the whole sky (Pinto et al., 2020), (b) the Electron Stack Detector (JUICE-RADEM-ESD) which has a full opening angle of 15° and will observe ~ 0.3 – ~ 40 MeV electrons with eight measurement channels (possibly integral), including six channels that will be sensitive only to > 1 MeV electrons (see Figure 7.17 of Socha (2021)).

The observation of MeV electrons by JUICE-RADEM-ESD may significantly improve upon the Galileo-EPD dataset for three reasons. First, as an engineering sensor, RADEM will always be switched on, unlike the record-mode of Galileo-EPD, and will therefore provide larger coverage in time and space than EPD. Secondly, the 15° opening angle of RADEM-ESD will better resolve the anisotropy of > 10 MeV electrons than the corresponding 45° -wide EPD telescope. Thirdly, the 6 RADEM integral channels that will observe MeV electrons will cover a larger energy range than Galileo-EPD.

However, JUICE will be a 3-axis stabilized spacecraft, so JUICE-RADEM-ESD will most of the time not inform on the anisotropy of > 1 MeV electrons. During JUICE roll maneuvers (for instance for magnetometer calibration), MeV electron PADs will be accumulated in a manner similar to what Cassini did at Saturn, with one

spacecraft rotation possibly taking hours. Such a slow rotation rate will enable RADEM to accumulate sufficient counts to provide reliable 1–2 hr-averaged observations of MeV electron PADs. JUICE will unlikely be able to spin with a period of 20 s or less as Galileo did, and will therefore not help to decipher the spatio-temporal structuring of MeV electron PADs in the middle and outer magnetosphere.

Ultimately, the only way to disruptively push forward our understanding of the uncharted MeV electrons in the Jovian magnetosphere is the in-situ observation of direction-resolved and energy-resolved (as opposed to integral) fluxes at these extreme energies. This observational objective calls for a specific instrumentation that could fly onboard any mission going to Jupiter. The observation of MeV electron PADs could also be one of the observational objectives of a space mission entirely dedicated to the magnetosphere and radiation belts of Jupiter (Clark et al., 2021; Nénon et al., 2021; Roussos et al., 2021).

Data Availability Statement

Galileo-EPD and ancillary data used in this work can be accessed in the archive available at <https://github.com/fundamental-technologies-llc/galileo-issues-repository>. This github repository contains in particular all numerical values of electron fluxes and pitch angles presented in this article. The individual Galileo spin plots of electron pitch angle distributions (PADs) generated in the present study, PAD spectrograms and count rate time series are available in the repository published at <https://doi.org/10.6084/m9.figshare.20180222.v1>.

Acknowledgments

We thank Drew Turner (JHU-APL) for discussions on the possible origins of pancake distributions. We thank Dimitrios Millas (University College London) for discussions on equatorial magnetic curvature scattering. Q. Nénon acknowledges support from the ESA postdoctoral fellowship, which funded the research presented in this article. The work of L. P. Miller was funded by NASA contract 80NSSC18P2239 for the Planetary Data Archiving, Restoration, and Tools (PDART) program. L. Liuzzo acknowledges NASA Solar System Workings Grant 80NSSC21K0152 and NASA New Frontiers Data Analysis Program Grant 80NSSC21K0823.

References

- Achilleos, N., Guio, P., Hardy, F., Paranicas, C., & Sorba, A. M. (2021). The Magnetodisk regions of Jupiter and Saturn. *Magnetospheres in the Solar System*, 453–469. <https://doi.org/10.1002/9781119815624.ch29>
- Allegri, F., Gladstone, G. R., Hue, V., Clark, G., Szalay, J. R., Kurth, W. S., et al. (2020). First report of electron measurements during a Europa footprint tail crossing by Juno. *Geophysical Research Letters*, 47(18), e2020GL089732. <https://doi.org/10.1029/2020gl089732>
- Allegri, F., Mauk, B., Clark, G., Gladstone, G. R., Hue, V., Kurth, W. S., et al. (2020). Energy flux and characteristic energy of electrons over Jupiter's main auroral emission. *Journal of Geophysical Research: Space Physics*, 125(4), e2019JA027693. <https://doi.org/10.1029/2019ja027693>
- Becker, H. N., Santos-Costa, D., Jørgensen, J. L., Denver, T., Adriani, A., Mura, A., et al. (2017). Observations of MeV electrons in Jupiter's innermost radiation belts and polar regions by the Juno radiation monitoring investigation: Perijoves 1 and 3. *Geophysical Research Letters*, 44(10), 4481–4488. <https://doi.org/10.1002/2017gl073091>
- Bhattacharya, B., Thorne, R. M., & Williams, D. J. (2001). On the energy source for diffuse Jovian auroral emissivity. *Geophysical Research Letters*, 28(14), 2751–2754. <https://doi.org/10.1029/2000gl012616>
- Birmingham, T. J. (1982). Charged particle motions in the distended magnetospheres of Jupiter and Saturn. *Journal of Geophysical Research*, 87(A9), 7421–7430. <https://doi.org/10.1029/ja087ia09p07421>
- Birmingham, T. J. (1984). Pitch angle diffusion in the Jovian magnetodisc. *Journal of Geophysical Research*, 89(A5), 2699–2707. <https://doi.org/10.1029/ja089ia05p02699>
- Bonfond, B., Gladstone, G. R., Grodent, D., Gérard, J. C., Greathouse, T. K., Hue, V., et al. (2018). Bar code events in the Juno-UVS data: Signature ~ 10 MeV electron microbursts at Jupiter. *Geophysical Research Letters*, 45(22), 12–108. <https://doi.org/10.1029/2018gl080490>
- Carbary, J. F., Mitchell, D. G., Kollmann, P., Krupp, N., Roussos, E., & Dougherty, M. K. (2018). Energetic electron pitch angle distributions during the Cassini final orbits. *Geophysical Research Letters*, 45(7), 2911–2917. <https://doi.org/10.1002/2018gl077656>
- Carbary, J. F., Mitchell, D. G., Paranicas, C., Roelof, E. C., Krimigis, S. M., Krupp, N., et al. (2011). Pitch angle distributions of energetic electrons at Saturn. *Journal of Geophysical Research*, 116(A1). <https://doi.org/10.1029/2010ja015987>
- Carlton, A., Pich, M. D. S. S., Kim, W., Jun, I., & Cahoy, K. (2018). Using the Galileo solid-state imaging instrument as a sensor of Jovian energetic electrons. *IEEE Transactions on Nuclear Science*, 66(1), 255–261.
- Clark, G., Kollman, P., Li, W., Jaynes, A., Blum, L., Marshall, R., et al. (2021). Jupiter's global magnetic environment and radiation observatory (JUGGERNOT): A mission to the solar system's greatest particle accelerator. *Talk at the 2021 AGU fall meeting*.
- Clark, G., Paranicas, C., Santos-Costa, D., Livi, S., Krupp, N., Mitchell, D. G., et al. (2014). Evolution of electron pitch angle distributions across Saturn's middle magnetospheric region from MIMI/LEMMS. *Planetary and Space Science*, 104, 18–28. <https://doi.org/10.1016/j.pss.2014.07.004>
- Connerney, J. E., Acuña, M. H., Ness, N. F., & Satoh, T. (1998). New models of Jupiter's magnetic field constrained by the Io flux tube footprint. *Journal of Geophysical Research*, 103(A6), 11929–11939. <https://doi.org/10.1029/97ja03726>
- Connerney, J. E. P., Timmins, S., Hecceg, M., & Joergensen, J. L. (2020). A Jovian magnetodisc model for the Juno era. *Journal of Geophysical Research: Space Physics*, 125(10), e2020JA028138. <https://doi.org/10.1029/2020ja028138>
- De Soria-Santacruz, M., Garrett, H. B., Evans, R. W., Jun, I., Kim, W., Paranicas, C., & Drozdov, A. (2016). An empirical model of the high-energy electron environment at Jupiter. *Journal of Geophysical Research: Space Physics*, 121(10), 9732–9743.
- Eviatar, A., Williams, D. J., Paranicas, C., McEntire, R. W., Mauk, B. H., & Kivelson, M. G. (2000). Trapped energetic electrons in the magnetosphere of Ganymede. *Journal of Geophysical Research*, 105(A3), 5547–5553. <https://doi.org/10.1029/1999ja000450>
- Garrett, H. B., & Jun, I. (2021). First adiabatic invariants and phase space densities for the Jovian electron and proton radiation belts—Galileo and GIRE3 estimates. *Journal of Geophysical Research: Space Physics*, 126(1), e2020JA028593. <https://doi.org/10.1029/2020ja028593>
- Grasset, O., Dougherty, M. K., Coustenis, A., Bunce, E. J., Erd, C., Titov, D., et al. (2013). Jupiter ICY moons Explorer (JUICE): An ESA mission to orbit Ganymede and to characterise the Jupiter system. *Planetary and Space Science*, 78, 1–21. <https://doi.org/10.1016/j.pss.2012.12.002>
- Han, S., Murakami, G., Kita, H., Tsuchiya, F., Tao, C., Misawa, H., et al. (2018). Investigating solar wind-driven electric field influence on long-term dynamics of Jovian synchrotron radiation. *Journal of Geophysical Research: Space Physics*, 123(11), 9508–9516. <https://doi.org/10.1029/2018ja025849>

- Hao, Y. X., Sun, Y. X., Roussos, E., Liu, Y., Kollmann, P., Yuan, C. J., et al. (2020). The formation of saturn's and jupiter's electron radiation belts by magnetospheric electric fields. *The Astrophysical Journal Letters*, 905(1), L10. <https://doi.org/10.3847/2041-8213/abca3f>
- Jun, I., Ratliff, J. M., Garrett, H. B., & McEntire, R. W. (2002). Monte Carlo simulations of the Galileo energetic particle detector. *Nuclear Instruments and Methods in Physics Research Section A: Accelerators, Spectrometers, Detectors and Associated Equipment*, 490(3), 465–475. [https://doi.org/10.1016/s0168-9002\(02\)01072-0](https://doi.org/10.1016/s0168-9002(02)01072-0)
- Katoh, Y., Tsuchiya, F., Miyoshi, Y., Morioka, A., Misawa, H., Ujiie, R., et al. (2011). Whistler mode chorus enhancements in association with energetic electron signatures in the Jovian magnetosphere. *Journal of Geophysical Research*, 116(A2). <https://doi.org/10.1029/2010ja016183>
- Khurana, K. K., & Schwarzl, H. K. (2005). Global structure of Jupiter's magnetospheric current sheet. *Journal of Geophysical Research*, 110(A7). <https://doi.org/10.1029/2004ja010757>
- Kivelson, M. G., Khurana, K. K., & Volwerk, M. (2002). The permanent and inductive magnetic moments of Ganymede. *Icarus*, 157(2), 507–522. <https://doi.org/10.1006/icar.2002.6834>
- Kivelson, M. G., Warnecke, J., Bennett, L., Joy, S., Khurana, K. K., Linker, J. A., et al. (1998). Ganymede's magnetosphere: Magnetometer overview. *Journal of Geophysical Research*, 103(E9), 19963–19972. <https://doi.org/10.1029/98je00227>
- Kollmann, P., Paranicas, C., Clark, G., Roussos, E., Lagg, A., & Krupp, N. (2016). The vertical thickness of Jupiter's Europa gas torus from charged particle measurements. *Geophysical Research Letters*, 43(18), 9425–9433. <https://doi.org/10.1002/2016gl070326>
- Kollmann, P., Roussos, E., Paranicas, C., Woodfield, E. E., Mauk, B. H., Clark, G., et al. (2018). Electron acceleration to MeV energies at jupiter and saturn. *Journal of Geophysical Research: Space Physics*, 123(11), 9110–9129. <https://doi.org/10.1029/2018ja025665>
- Kollmann, P., Roussos, E., Paranicas, C., Woodfield, E. E., Mauk, B. H., Clark, G., & Vandegriff, J. (2019). Galileo/EPD user guide. Retrieved from http://sd-www.jhuapl.edu/Galileo_EPDPD/userguide/GaliUser_v25C.pdf
- Li, W., Ma, Q., Shen, X. C., Zhang, X. J., Mauk, B. H., Clark, G., et al. (2021). Quantification of diffuse auroral electron precipitation driven by whistler mode waves at jupiter. *Geophysical Research Letters*, 48(19), e2021GL095457. <https://doi.org/10.1029/2021gl095457>
- Li, W., Ma, Q., Thorne, R. M., Bortnik, J., Zhang, X. J., Li, J., et al. (2016). Radiation belt electron acceleration during the 17 March 2015 geomagnetic storm: Observations and simulations. *Journal of Geophysical Research: Space Physics*, 121(6), 5520–5536. <https://doi.org/10.1002/2016ja022400>
- Liuzzo, L., Feyerabend, M., Simon, S., & Motschmann, U. (2015). The impact of Callisto's atmosphere on its plasma interaction with the Jovian magnetosphere. *Journal of Geophysical Research: Space Physics*, 120(11), 9401–9427. <https://doi.org/10.1002/2015ja021792>
- Liuzzo, L., Poppe, A. R., Paranicas, C., Nénon, Q., Fatemi, S., & Simon, S. (2020). Variability in the energetic electron bombardment of Ganymede. *Journal of Geophysical Research: Space Physics*, 125(9), e2020JA028347. <https://doi.org/10.1029/2020ja028347>
- Liuzzo, L., Simon, S., Feyerabend, M., & Motschmann, U. (2017). Magnetic signatures of plasma interaction and induction at Callisto: The Galileo C21, C22, C23, and C30 flybys. *Journal of Geophysical Research: Space Physics*, 122(7), 7364–7386. <https://doi.org/10.1002/2017ja024303>
- Liuzzo, L., Simon, S., & Regoli, L. (2019). Energetic electron dynamics near Callisto. *Planetary and Space Science*, 179, 104726. <https://doi.org/10.1016/j.pss.2019.104726>
- Long, M., Ni, B., Cao, X., Gu, X., Kollmann, P., Luo, Q., et al. (2022). Losses of radiation belt energetic particles by encounters with four of the inner moons of Jupiter. *Journal of Geophysical Research: Planets*, 127(2), e2021JE007050. <https://doi.org/10.1029/2021je007050>
- Ma, Q., Li, W., Zhang, X. J., & Bagenal, F. (2020). Energetic electron scattering due to whistler mode chorus waves using realistic magnetic field and density models in Jupiter's magnetosphere. *Journal of Geophysical Research: Space Physics*, 125(8), e2020JA027968. <https://doi.org/10.1029/2020ja027968>
- Ma, Q., Li, W., Zhang, X. J., Shen, X. C., Daly, A., Bortnik, J., et al. (2021). Energetic electron distributions near the magnetic equator in the Jovian plasma sheet and outer radiation belt using Juno observations. *Geophysical Research Letters*, 48(24), e2021GL095833. <https://doi.org/10.1029/2021gl095833>
- Mauk, B. H., Clark, G., Gladstone, G. R., Kotsiaros, S., Adriani, A., Allegrini, F., & Rymer, A. M. (2020). Energetic particles and acceleration regions over Jupiter's polar cap and main aurora: A broad overview. *Journal of Geophysical Research: Space Physics*, 125(3), e2019JA027699. <https://doi.org/10.1029/2019ja027699>
- Mauk, B. H., & Fox, N. J. (2010). Electron radiation belts of the solar system. *Journal of Geophysical Research*, 115(A12). <https://doi.org/10.1029/2010ja015660>
- Mauk, B. H., Haggerty, D. K., Jaskulek, S. E., Schlemm, C. E., Brown, L. E., Cooper, S. A., & Stokes, M. R. (2017a). The Jupiter energetic particle detector instrument (JEDI) investigation for the Juno mission. *Space Science Reviews*, 213(1), 289–346. <https://doi.org/10.1007/s11214-013-0025-3>
- Mauk, B. H., Haggerty, D. K., Paranicas, C., Clark, G., Kollmann, P., Rymer, A. M., et al. (2017b). Juno observations of energetic charged particles over Jupiter's polar regions: Analysis of monodirectional and bidirectional electron beams. *Geophysical Research Letters*, 44(10), 4410–4418. <https://doi.org/10.1002/2016gl072286>
- Mauk, B. H., Haggerty, D. K., Paranicas, C., Clark, G., Kollmann, P., Rymer, A. M., et al. (2017c). Discrete and broadband electron acceleration in Jupiter's powerful aurora. *Nature*, 549(7670), 66–69. <https://doi.org/10.1038/nature23648>
- Mauk, B. H., & Saur, J. (2007). Equatorial electron beams and auroral structuring at Jupiter. *Journal of Geophysical Research*, 112(A10). <https://doi.org/10.1029/2007ja012370>
- Mauk, B. H., Williams, D. J., McEntire, R. W., Khurana, K. K., & Roederer, J. G. (1999). Storm-like dynamics of Jupiter's inner and middle magnetosphere. *Journal of Geophysical Research*, 104(A10), 22759–22778. <https://doi.org/10.1029/1999ja000097>
- Miller, L. P., Manweiler, J., Sittler, E., Cooper, J., & Kollmann, P. (2021). *New high-level Galileo energetic particle detector and magnetic field dataset*. AGU Fall Meeting. Poster at the 2021.
- Nénon, Q., & André, N. (2019). Evidence of Europa neutral gas torii from energetic sulfur ion measurements. *Geophysical Research Letters*, 46(7), 3599–3606.
- Nénon, Q., Clark, G., Jun, I., Kollmann, P., Liuzzo, L., Mauk, B., et al. (2021). Open science questions and missing measurements in the radiation belts of Jupiter. *Bulletin of the American Astronomical Society*, 53(4), 088. <https://doi.org/10.3847/25c2cfef.fb50005f>
- Nénon, Q., Sicard, A., & Bourdarie, S. (2017). A new physical model of the electron radiation belts of Jupiter inside Europa's orbit. *Journal of Geophysical Research: Space Physics*, 122(5), 5148–5167.
- Nénon, Q., Sicard, A., & Caron, P. (2018). The rings of Jupiter as seen by the electron and proton radiation belt model Salammbô. *Geophysical Research Letters*, 45(20), 10–838.
- Nordheim, T. A., Hand, K. P., & Paranicas, C. (2018). Preservation of potential biosignatures in the shallow subsurface of Europa. *Nature Astronomy*, 2(8), 673–679. <https://doi.org/10.1038/s41550-018-0499-8>
- Paranicas, C., Hibbitts, C. A., Kollmann, P., Ligier, N., Hendrix, A. R., Nordheim, T. A., et al. (2018). Magnetospheric considerations for solar system ice state. *Icarus*, 302, 560–564. <https://doi.org/10.1016/j.icarus.2017.12.013>

- Paranicas, C., Mauk, B. H., Haggerty, D. K., Clark, G., Kollmann, P., Rymer, A. M., et al. (2018). Intervals of intense energetic electron beams over Jupiter's poles. *Journal of Geophysical Research: Space Physics*, *123*(3), 1989–1999. <https://doi.org/10.1002/2017ja025106>
- Paranicas, C., McEntire, R. W., Cheng, A. F., Lagg, A., & Williams, D. J. (2000). Energetic charged particles near Europa. *Journal of Geophysical Research*, *105*(A7), 16005–16015. <https://doi.org/10.1029/1999ja000350>
- Paranicas, C., Regoli, L., Ligier, N., Nordheim, T., & Hibbitts, K. (2021). Exogenic versus endogenic features of the planetary satellites. *Bulletin of the American Astronomical Society*, *53*(4), 017. <https://doi.org/10.3847/25c2cfcb.26167acd>
- Pinto, M., Gonçalves, P., Socha, P., Hajdas, W., Marques, A., & Pinto, J. C. (2020). Beam test results of the RADEM engineering model. *Nuclear Instruments and Methods in Physics Research Section A: Accelerators, Spectrometers, Detectors and Associated Equipment*, *958*, 162795. <https://doi.org/10.1016/j.nima.2019.162795>
- Roussos, E., Allanson, O., André, N., Bertucci, B., Branduardi-Raymont, G., Clark, G., et al. (2021). The in-situ exploration of Jupiter's radiation belts. *Experimental Astronomy*, 1–45.
- Roussos, E., Cohen, C., Kollmann, P., Pinto, M., Krupp, N., Gonçalves, P., & Dialynas, K. (2022). A source of very energetic oxygen located in Jupiter's inner radiation belts. *Science Advances*, *8*(2), eabm4234. <https://doi.org/10.1126/sciadv.abm4234>
- Rymer, A. M., Mauk, B. H., Hill, T. W., Paranicas, C., Mitchell, D. G., Coates, A. J., & Young, D. T. (2008). Electron circulation in Saturn's magnetosphere. *Journal of Geophysical Research*, *113*(A1). <https://doi.org/10.1029/2007ja012589>
- Sicard-Piet, A., Bourdarie, S., & Krupp, N. (2011). Jose: A new Jovian specification environment model. *IEEE Transactions on Nuclear Science*, *58*(3), 923–931. <https://doi.org/10.1109/tns.2010.2097276>
- Simpson, J. A., Anglin, J. D., Balogh, A., Burrows, J. R., Cowley, S. W. H., Ferrando, P., et al. (1992). Energetic charged-particle phenomena in the Jovian magnetosphere: First results from the Ulysses COSPIN collaboration. *Science*, *257*(5076), 1543–1550. <https://doi.org/10.1126/science.257.5076.1543>
- Socha, P. (2021). *Qualification of the RADEM instrument for the ESA JUICE mission*. PhD Thesis.
- Socha, P., Pinto, M., Hajdas, W., & Gonçalves, P. (2020). Beam tests of a prototype of the Radiation Hard Electron Monitor to be flown in the JUICE mission. *Journal of Instrumentation*, *15*(06), C06032. <https://doi.org/10.1088/1748-0221/15/06/c06032>
- Thorne, R. M., Williams, D. J., Zhang, L. D., & Stone, S. (1999). Energetic electron butterfly distributions near Io. *Journal of Geophysical Research*, *104*(A7), 14755–14766. <https://doi.org/10.1029/1999ja900132>
- Tomás, A., Woch, J., Krupp, N., Lagg, A., Glassmeier, K. H., Dougherty, M. K., & Hanlon, P. G. (2004). Changes of the energetic particles characteristics in the inner part of the Jovian magnetosphere: A topological study. *Planetary and Space Science*, *52*(5–6), 491–498.
- Williams, D. J. (2004). Energetic electron beams in Ganymede's magnetosphere. *Journal of Geophysical Research*, *109*(A9). <https://doi.org/10.1029/2004ja010521>
- Williams, D. J., & Mauk, B. (1997). Pitch angle diffusion at Jupiter's moon Ganymede. *Journal of Geophysical Research*, *102*(A11), 24283–24287. <https://doi.org/10.1029/97ja02260>
- Williams, D. J., Mauk, B., & McEntire, R. W. (1997b). Trapped electrons in Ganymede's magnetic field. *Geophysical Research Letters*, *24*(23), 2953–2956. <https://doi.org/10.1029/97gl03003>
- Williams, D. J., Mauk, B., & McEntire, R. W. (1998). Properties of Ganymede's magnetosphere as revealed by energetic particle observations. *Journal of Geophysical Research*, *103*(A8), 17523–17534. <https://doi.org/10.1029/98ja01370>
- Williams, D. J., Mauk, B. H., McEntire, R. W., Roelof, E. C., Armstrong, T. P., Wilken, B., et al. (1997a). Energetic particle signatures at Ganymede: Implications for Ganymede's magnetic field. *Geophysical Research Letters*, *24*(17), 2163–2166. <https://doi.org/10.1029/97gl01931>
- Williams, D. J., McEntire, R. W., Jaskulek, S., & Wilken, B. (1992). The Galileo energetic particles detector. *Space Science Reviews*, *60*(1), 385–412. https://doi.org/10.1007/978-94-011-2512-3_16
- Williams, D. J., & Thorne, R. M. (2003). Energetic particles over Io's polar caps. *Journal of Geophysical Research*, *108*(A11). <https://doi.org/10.1029/2003ja009980>
- Woodfield, E. E., Horne, R. B., Glauert, S. A., Menietti, J. D., & Shprits, Y. Y. (2014). The origin of Jupiter's outer radiation belt. *Journal of Geophysical Research: Space Physics*, *119*(5), 3490–3502. <https://doi.org/10.1002/2014ja019891>
- Yuan, C. J., Roussos, E., Wei, Y., Krupp, N., Sun, Y. X., & Hao, Y. X. (2021). Cassini observation of relativistic electron butterfly distributions in Saturn's inner radiation belts: Evidence for acceleration by local processes. *Geophysical Research Letters*, *48*(14), e2021GL092690. <https://doi.org/10.1029/2021gl092690>